Modeling the Decomposition Mechanism of Artemisinin

Pamela Moles, Mónica Oliva, and Vicent S. Safont*

Departament de Ciències Experimentals, Universitat Jaume I, 12080 Castelló, Spain

Received: December 20, 2005; In Final Form: March 13, 2006

A theoretical study on artemisinin decomposition mechanisms is reported. The calculations have been done at the HF/3-21G and B3LYP/6-31G(d,p) theoretical levels, by using 6,7,8-trioxybicyclo[3.2.2]nonane as the molecular model for artemisinin, and a hydrogen atom, modeling the single electron transfer from heme or Fe(II) in the highly acidic parasite's food vacuole, as inductor of the initial peroxide bond cleavage. All relevant stationary points have been characterized, and the appearance of the final products can be explained in a satisfactory way. Several intermediates and radicals have been found as relatively stable species, thus giving support to the current hypothesis that some of these species can be responsible for the antimalarial action of artemisinin and its derivatives.

Introduction

Malaria is one of the most worrying infectious diseases currently affecting the human race. Forty percent of the world's population is at risk of malaria infection, and each year 100 million people experience a malarial illness that kills about 2.7 million of them (primarily African children).[1] There are four members of the *Plasmodium* genus that infect humans, via transmission through the bite of the Anofeles female mosquito.[2]

The parasite responsible for the majority of fatal malaria infections, *Plasmodium falciparum*, can kill patients in a matter of hours. Most strains of *P. falciparum* have now become resistant to chloroquine and other traditional antimalarials,[3,4] and this fact provides the reason for research for new drugs.

Artemisinin (*qinghaosu*, **1**, Scheme 1), which was isolated by Chinese chemists in the early 1970s from the ancient *Artemisia annua* (sweet wormwood) Chinese herbal remedy for fevers,[5] is the most relevant advance in the treatment of malaria disease in the last 20 years; artemisinin and some derivatives are the most potent and rapidly acting antimalarial drugs at hand nowadays.[6] Artemisinin is a sesquiterpene lactone with an endoperoxide group, and their unusual 1,2,4-trioxane ring system has been proven to be critical for the antimalarial activity.[1,7]

The mechanism of action of artemisinin is not clear, and it is still under debate.[3,8,9] Artemisinin and endoperoxide-based drugs have the ability to generate a range of different reactive intermediates, and many of these have been proposed as the mediators of the antimalarial activity of this class of drugs:

(a) The activation of the artemisinin peroxidic bond by iron(II)−heme can generate oxygen-centered radicals that could kill the parasite; this drug-mediated oxidative stress has been proposed on the basis of in vitro experiments with infected human red blood cells or with parasite membranes.[10] However, it has also been proposed that the parasite death in the presence of artemisinin is probably not due to nonspecific or random cell damage caused by freely diffusing oxygen radicals but might involve specific radicals and targets.[11,12]

(b) An acid-mediated opening of the peroxidic function of artemisinin, generating a hydroperoxide that would be the source of electrophilic oxygenating species, has also been suggested.[13] However, other authors have argued against an initial heterolytic cleavage mechanism on the basis of spin-trapping experiments that show that homolysis is the only route of artemisinin degradation with no evidence of heterolytic retro-Michael addition of the endoperoxide bridge.[14]

(c) The transfer of an oxygen atom from the peroxide function of artemisinin to a chelated iron ion to generate an Fe(IV)═O toxic species has also been proposed,[15] but several groups have contested this chemical mechanism.[16−18]

(d) The reductive cleavage of the peroxide bond in artemisinin, prompted by ferrous iron (in the form of heme or iron(II) salts) can form oxygen-centered radicals[19] which, in turn, can lead to the formation of carbon-centered radicals.[20] These are now widely accepted (although sometimes questioned[6,21]) as key intermediates in a series of chemical reactions leading from antimalarial trioxane to various intermediates, one or more of which could kill the malaria parasites.[4] Definitive evidence for the generation of carbon radical intermediates during ferrous-mediated endoperoxide degradation of artemisinin and its derivatives has been provided by EPR spin-trapping techniques,[22−24] but the question if these radicals are simply intermediates to other species, like carbocations, responsible for the observed alkylation of proteins, still remain unresolved.[3,25]

On the other hand, several molecular targets have been proposed for the reactive intermediates generated from artemisinin and its derivatives:

(a) Alkylation of heme to form heme−artemisinin adducts has been proposed to result in the prevention of heme polymerization to nontoxic hemozoin, thus leading to the parasite death by a mechanism similar to that proposed for the chloroquine-based antimalarials.[16,26−28] However, it is not clear if the inhibition of the heme polymerization is related to the antimalarial mode of action of this class of drugs, and some recent studies suggest that the activity of artemisinins does not require heme.[12,29−31]

(b) Alkylation of some specific parasite proteins when artemisinin or other active trioxanes were incubated within human red blood cells infected by *P. falciparum* has also been reported.[32−34] Another possible target protein is the translationally controlled tumor protein.[35,36]

(c) Artemisinin has also been proposed to be involved in the specific inhibition of malarial protease activity.[37]

(d) Recently, compelling evidence has been provided that artemisinin acts by inhibiting PfATP6, the sarco/endoplasmic reticulum Ca^{2+}-ATPase (SERCA) orthologue of *P. falciparum*.[12]

10.1021/jp0574089 CCC: $33.50
Published on Web 05/06/2006

SCHEME 1

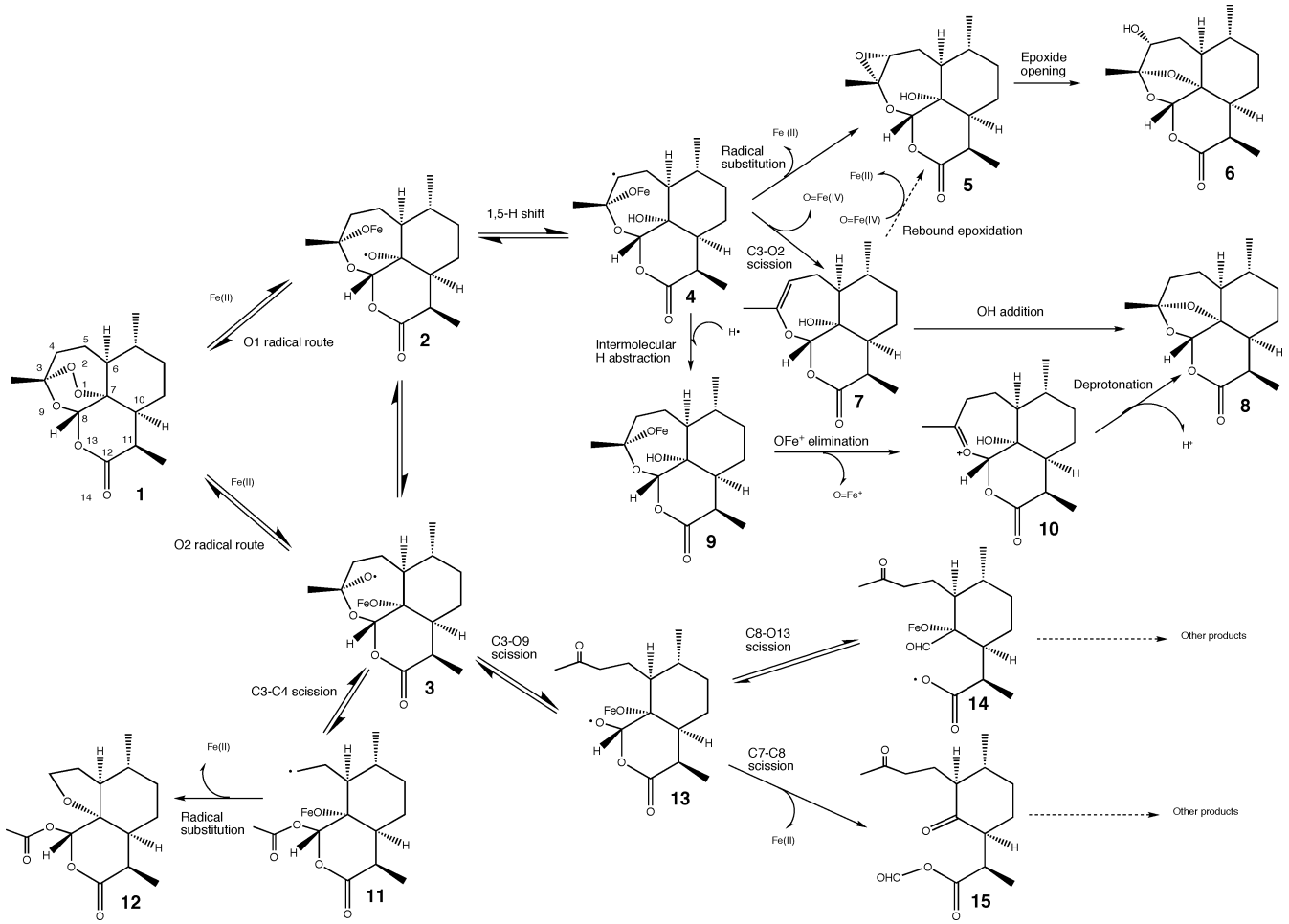

Overall, the weight of evidence and the fact that resistance has not yet developed to the artemisinins suggest that the drugs do not exert their antimalarial effects by hitting a single biological target but rather by simultaneously hitting several targets with very high precision and efficiency.[3,30]

In the past 2 decades, a large number of papers have been published dealing with the artemisinin antimalarial activity, and a significant progress has been made in the elucidation of the chemical mechanisms of action. Among the published papers, some pioneering theoretical investigations can be found.

The first theoretical investigation on the mechanism of decomposition of trioxanes was made by Gu et al.[7] within the unified mechanistic framework for the Fe(II) induced cleavage of artemisinin[15,23] (Scheme 1). The mechanism sketched in Scheme 1, adapted from ref 23, is nowadays generally accepted for the ferrous ion induced cleavage of 1,2,4-trioxanes. Gu et al. studied the intramolecular 1,5-hydrogen shift (from **2** to **4**) and the homolytic C−C cleavage (from **3** to **11**) steps by using the molecular model 6,7,8-trioxybicyclo[3.2.2]nonane (**1m**, Scheme 2) at the B3LYP/6-31G(d,p) level. Recently, Drew et al. have used artemisinin itself (**1**) to study the same steps at the same theoretical level,[38] and Tonmunphean et al.[39] reported also these steps at IMOMO (B3LYP/6-31G(d,p)/HF/3-21G), by using artemisinin, dihydroartemisinin, and deoxoartemisinin as molecular models. On the other hand, Taranto and co-workers[8,40] studied the processes at the semiempirical AM1 and PM3 levels by using **1** as a model, and the structures and energies of **2**, **4**, **5**, **6**, **3**, **11**, **12**, **13**, **14**, and **15** were obtained. Besides the different model size used in these studies, it is worth noting that, in some of them,[7,38,39] a hydrogen atom is used instead of the ferrous ion so that the oxygen- and carbon-centered model radicals are neutral, while in the Taranto's work[8,40] an electron is chosen so that the oxygen- and carbon-centered model radicals are anionic. This difference affects also the subsequent steps in the sense that to reach the proposed final species appearing in the mechanism (cf., **5**, **6**, **7**, **8**, **12**, and **15**, see Scheme 1), either a hydrogen atom,[7] or an electron,[8] has to be eliminated from the model molecules.

Very recently, a work by Taranto et al.[41] has appeared reporting geometries at B3LYP/6-31G(d), and energies at B3LYP/6-31+G(d,p)//B3LYP/6-31G(d) levels, of structures **2**, **4**, **3**, **11**, and the two corresponding transition structures (TSs), and also some information on the energetics of **5** and **6**. The authors use **1** as the molecular model and an H atom instead of the iron(III). An electron is also used: the authors calculate neutral radicals as well as anion radicals, although the results better agree with experiment when using the neutral ones, which is not surprising because of the highly acidic media in which the processes take place, that favors protonation of the putative anions as they are formed.

In the present paper, we report a theoretical study modeling the whole proposed mechanism for the decomposition of artemisinin[15,23] with the aim of revealing the details of the structures, stability, and processes involved in the postulated steps, and contributing to a better understanding of the rearrangement of endoperoxides at the molecular level that may lead to the development of more potent and therapeutically efficient drugs than those already available.

SCHEME 2

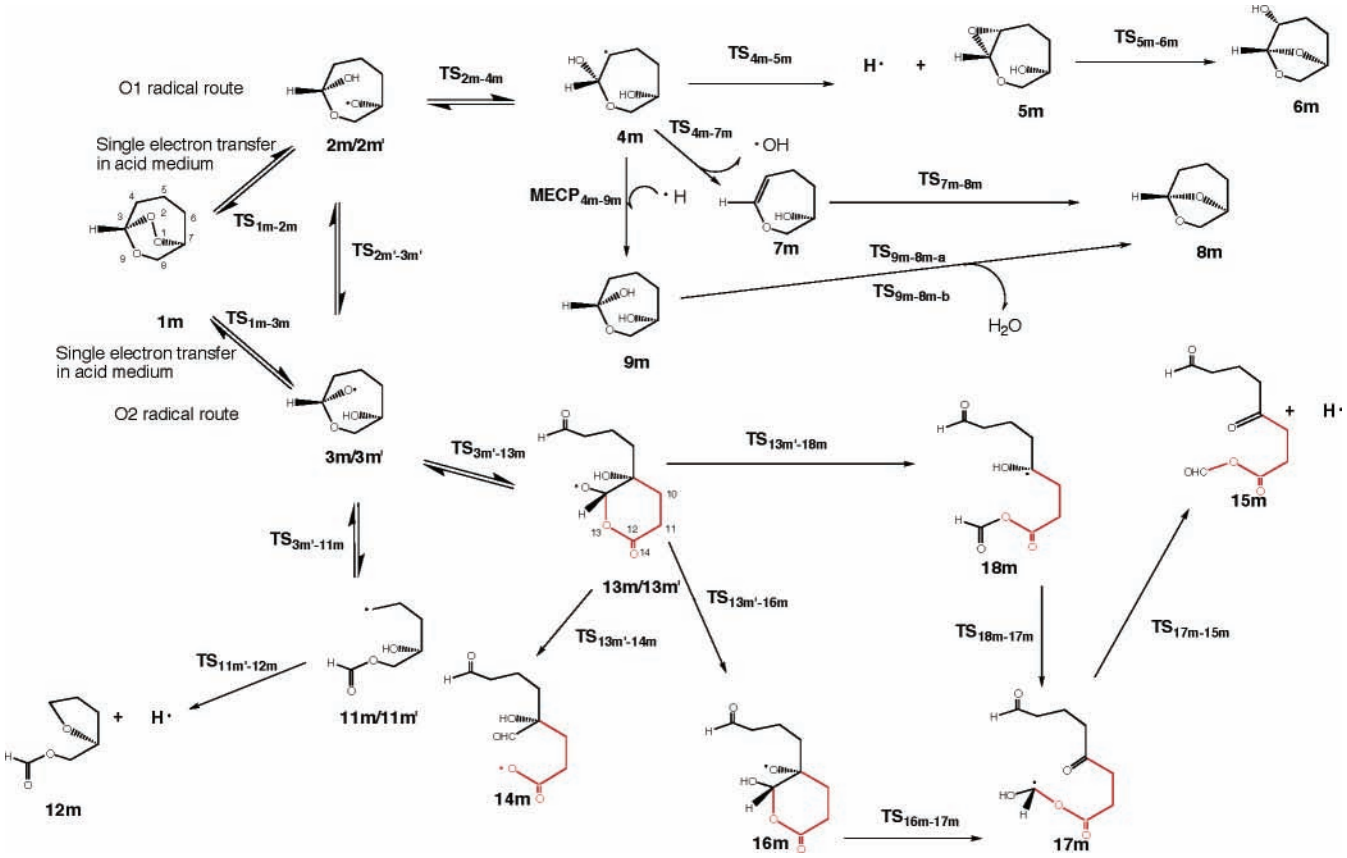

Computational Methods and Models

Following the work of Gu et al.,[7] we have used **1m** as the molecular model and an H atom to induce the initial peroxide cleavage. In the real system a single electron transfer prompts for the peroxide bond cleavage. However, due to the high acidity in the parasite's food vacuole, the putative radical anions formed should be protonated as they are formed. Hence, the use of an H atom modeling the Fe(II) approaching the O−O bridge and forming an O−H bond after peroxide cleavage accounts for the actual situation.[39,41] We have characterized all relevant stationary points, minima, and TSs shown in Scheme 2, at the HF/3-21G theoretical level. It is worth noting that the small model used is not adequate for some later steps in the mechanism (cf., steps from **13m** onward), because the neighbor atoms have to be taken into account at those steps. Hence, we have conveniently enlarged the molecular model as can be seen in Scheme 2, to complete the investigations of those later steps. Then, we have further refined the calculated structures at the B3LYP/6-31G(d,p) level, to check the accuracy of the HF approach and to obtain more reliable values for the energetic parameters.

All stationary points have been characterized as minima or TSs by means of a vibrational analysis. All the wavenumbers obtained for the minima are positive, while in the case of the TS, one and only one wavenumber is imaginary. This unique imaginary frequency, associated to the transition vector (TV),[42] that is, the eigenvector associated with the unique negative eigenvalue of the force constant matrix, describes the atomic motion at the TS and can be used to trace the intrinsic reaction coordinate (IRC)[43] pathway that connects reactants and products. The Gaussian98[44] program package was used for all the calculations.

The unrestricted (UHF, UB3LYP) formalisms were used for the species with unpaired electrons. The doublet nature of the radicals was confirmed by the values of the S^2 operator. All calculated radicals showed S^2 values before annihilation of the first spin contaminant (B3LYP/6-31G(d,p) level) between 0.7739 and 0.7527, which are very close to the true doublet state S^2 value of 0.75. Spin densities were obtained summing up the diagonal terms of the spin density matrix for each atom.

Results and Discussion

The cleavage of **1** with $FeSO_4$ in aqueous CH_3CN gave two major products, **6** and **12**, in 67% and 25% yields, respectively, while **5** has been identified as a minor component (1−2% yield).[23] On the other hand, if the cleavage of **1** is conducted by using $FeBr_2$ in THF/1,4-cyclohexadiene, three major products were obtained, namely, **8**, **12**, and **6**, in 71%, 16.7%, and 4.2% yields, respectively.[45]

To account for these and many other experimental observations, the unified decomposition mechanism shown in Scheme 1[15,23] has been proposed for the artemisinin decomposition process. It begins with the Fe(II)-mediated cleavage of the endoperoxide bridge, through a single electron transfer from the Fe(II) ion to the peroxy bond, yielding two radical anions ion-paired with the resulting Fe(III): **2** (O1 radical) and **3** (O2 radical). Each one of the radicals has its own routes, the O1 radical route starting from **2** and the O2 radical route starting from **3**, to evolve further and give the final products.

The O1 radical route has been suggested to render the products, **5**, **6**, **7**, and **8**. The O2 radical route can explain the appearance of **12**, among other possible decomposition products. The radicals **2** and **3** were postulated to be rapidly interchangeable, and we have for the first time obtained a TS modeling such interconversion, see below.

From the Starting 1,2,4-Trioxane to the Carbon-Centered Radicals. As stated above, we have used **1m** as the molecular

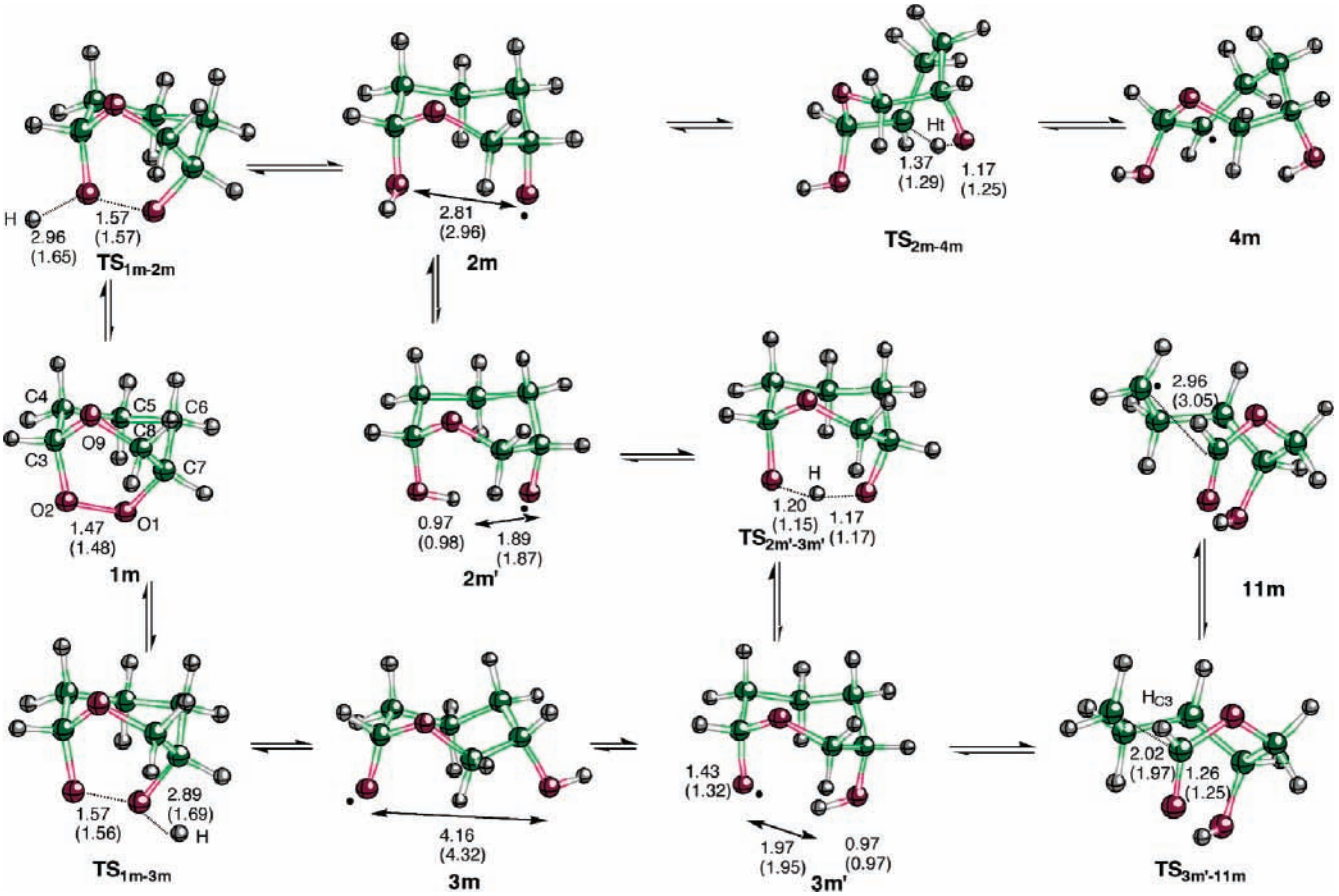

Figure 1. Stationary points **1m**, **2m**, **2m′**, **3m**, **3m′**, **4m**, **11m**, $\mathbf{TS_{1m-2m}}$, $\mathbf{TS_{2m'-3m'}}$, $\mathbf{TS_{1m-3m}}$, $\mathbf{TS_{2m-4m}}$, and $\mathbf{TS_{3m'-11m}}$. Selected geometric parameters at HF/3-21G and B3LYP/6-31G(d,p) (in parentheses) are shown. The atom numbering is also indicated.

model for **1** (Scheme 2). The peroxide opening induced by a hydrogen atom can give either **2m** or **3m**, from which the O1 and O2 radical routes, respectively, can be modeled. From **2m**, an intramolecular 1,5-hydrogen shift produces a secondary carbon-centered radical **4m** which may have several pathways for further reaction. From **3m**, via C3−C4 scission, radical **11m** can be attained.

In Figure 1 the stationary points **1m**, **2m**, **2m′**, **3m**, **3m′**, **4m**, and **11m**, as well as $\mathbf{TS_{1m-2m}}$, $\mathbf{TS_{1m-3m}}$, $\mathbf{TS_{2m'-3m'}}$, $\mathbf{TS_{2m-4m}}$, and $\mathbf{TS_{3m'-11m}}$, are depicted, and some geometric parameters are indicated. The energetics of these structures are reported as Supporting Information. We have calculated the reference energy as the sum of the energies of **1m** and the H atom that, as commented above, accounts for the single electron transfer in the acidic parasite's food vacuole. In Figure 2, energy profiles are drawn from the energetic values.

As the H atom modeling the Fe(II) approaches O1 or O2, the O1−O2 distance in **1m** smoothly increases and the energy of the system slightly rises until $\mathbf{TS_{1m-2m}}$ or $\mathbf{TS_{1m-3m}}$ are reached. From $\mathbf{TS_{1m-2m}}$, the O1 radical **2m** is found. The O1−O2 bond has been broken, and the unpaired electron is localized mainly at the O1 atom. Thereafter, a 1−5 H shift, via $\mathbf{TS_{2m-4m}}$ with a small energy barrier of ca. 10 kcal/mol (B3LYP value, HF renders a barrier of ca. 32 kcal/mol), can yield the secondary C4 radical **4m**, that is found to be slightly more stable than **2m** when the B3LYP approach is used.

In addition, we have found that a small conformational change is possible from **2m**, yielding **2m′**. From this point, a hydrogen exchange between O2 and O1, via $\mathbf{TS_{2m'-3m'}}$, gives rise to the O2-centered radical **3m′**. This TS is the first theoretical evidence that the O1 and O2 radical routes can be interconnected, giving support to the previous proposals about this fact. In the real system, the Fe(III) ion has to move from one oxygen to another, instead of an H atom. Preliminary calculations from our group, not shown here, including the ferric ion, suggest that a TS describing this interchange process does exists. The O2 pathway is thermodynamically favored according to the results of the calculations at the B3LYP level on the model system, suggesting an initial preference for such a route.

The species **3m′** can also be attained starting from **1m**, via $\mathbf{TS_{1m-3m}}$ and **3m**, after a conformational change. Finally, the C3−C4 scission of **3m′**, via $\mathbf{TS_{3m'-11m}}$, leads to the primary C4 carbon radical **11m**, which is the more stable structure within these initial steps.

The two computational approaches used, B3LYP/6-31G (d,p) and HF/3-21G, render quite similar geometries, the main difference being the calculated distances of the H entering atom to O1 or O2 at $\mathbf{TS_{1m-2m}}$ or $\mathbf{TS_{1m-3m}}$, respectively. However, the energy description is different: HF results show **2m′** as the more stable species. A smoother profile is found by using the DFT-based approach; as it includes electron correlation, the B3LYP results can be given more confidence. The whole process from **1m** to either **4m** or **11m** is found to be highly exothermic, thus giving support to the proposed C-centered radical formation.

In Table 1, the S^2 operator values and the spin density on selected atoms are reported for the stationary points found. It is apparent that the B3LYP calculations are more adequate for describing the radicals than the HF ones, because the former show a significantly lower spin contamination and properly describe such species as doublets. The HF wave function is less accurate, and some residual spin contamination is found, mainly for the $\mathbf{TS_{1m-2m}}$, $\mathbf{TS_{1m-3m}}$, and $\mathbf{TS_{3m'-11m}}$. The B3LYP values

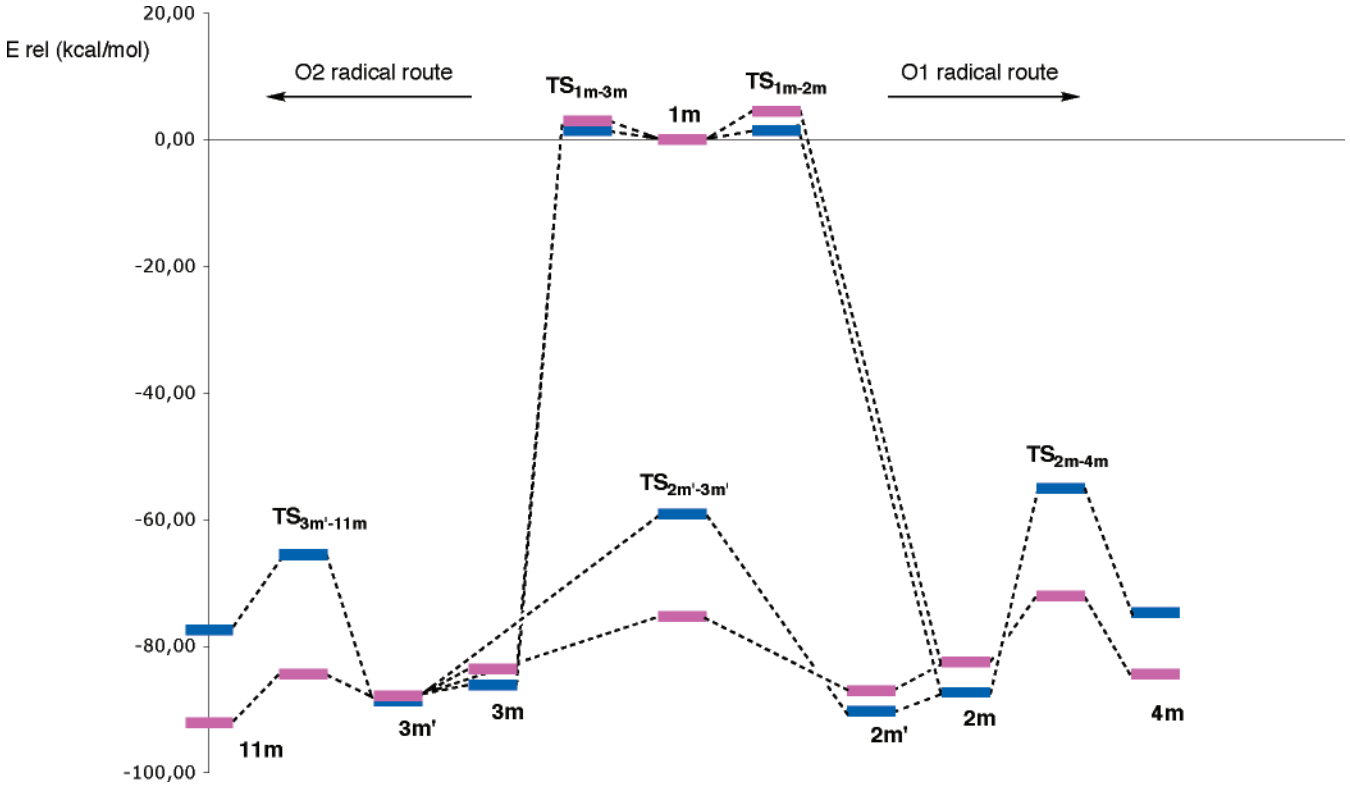

Figure 2. Energy profiles for the steps leading from **1m** to **4m** and **11m**. HF and B3LYP results are indicated in blue and pink colors, respectively.

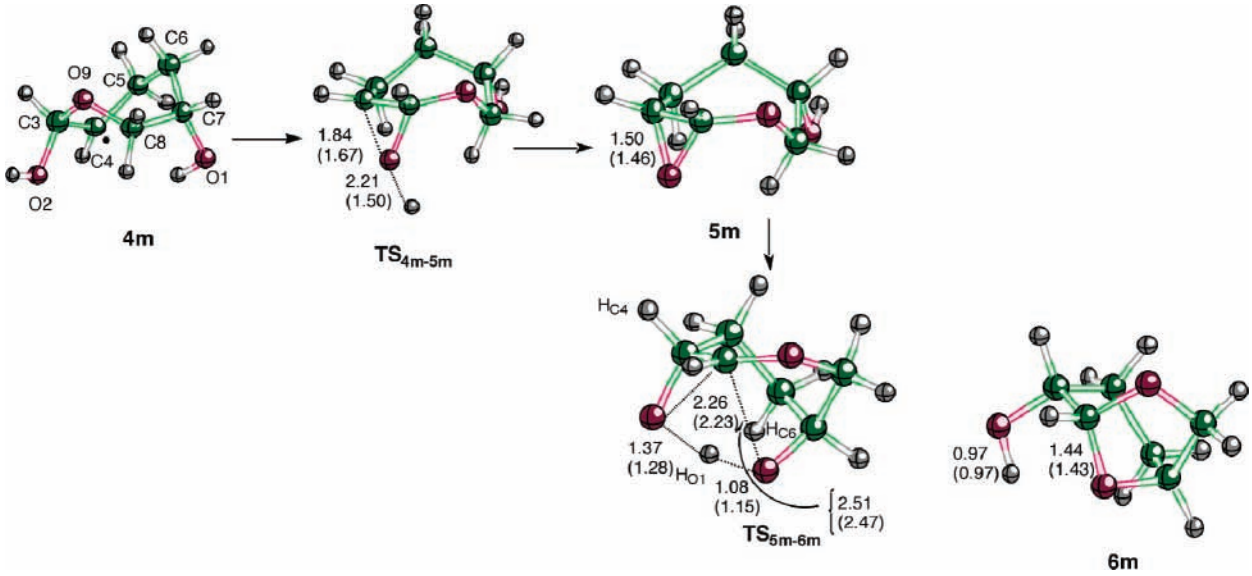

Figure 3. Stationary points **4m**, **5m**, **6m**, $\mathbf{TS_{4m-5m}}$, and $\mathbf{TS_{5m-6m}}$. Selected geometric distances (Å) at HF/3-21G and B3LYP/6-31G(d,p) (in parentheses) are shown. The atom numbering is also indicated.

show the spin density at $\mathbf{TS_{1m-2m}}$ and $\mathbf{TS_{1m-3m}}$ on the H atom being incorporated to the model molecule, with some delocalization to the O1 and O2 atoms, respectively. At **2m** and **2m′** the unpaired electron is mainly found on the O1 atom, while at **3m** and **3m′** it is mainly localized on the O2 atom. At $\mathbf{TS_{2m'-3m'}}$ the spin density is found on both O1 and O2 atoms and not on the H atom being transferred. The $\mathbf{TS_{2m-4m}}$ show a situation with the radical character partitioned between C4 and O1, and at **4m** the unpaired electron is localized on C4, as expected. At $\mathbf{TS_{3m'-11m}}$ a larger spin density is found on C4 than on O2, and hence this TS has a late character. Finally, at **11m** the unpaired electron is found on C4.

The imaginary frequencies, the negative eigenvalues, and the main components of the TVs for the TSs found are reported as Supporting Information. The $\mathbf{TS_{1m-2m}}$ and $\mathbf{TS_{1m-3m}}$ are associated to the O1−O2 breaking bond and H−O1 or H−O2 forming bonds, as expected. The two theoretical approaches used render a different fluctuation pattern: the HF results describe a situation in which the O1−O2 breaking dominates, because the H atom is still located far from the oxygen atom, while the B3LYP calculations describe a later situation, with the H atom closer to the corresponding oxygen. Accordingly, the imaginary frequencies are higher for the B3LYP results, because the H motion dominates.

For $\mathbf{TS_{2m'-3m'}}$, $\mathbf{TS_{2m-4m}}$, and $\mathbf{TS_{3m'-11m}}$, a very similar fluctuation pattern is described by the two theoretical approaches. The TSs are associated to the expected atom motions, and hence $\mathbf{TS_{2m'-3m'}}$ describes the H exchange between O1 and

TABLE 1: S^2 Operator Values for the Stationary Points Indicated[a]

	S^2		S		S^2		S
TS_{1m-2m}	0.9930 (0.7739)	H O1 O2	1.00 (0.82) 0.50 (0.19) −0.50 (−0.05)	**TS_{1m-3m}**	0.9893 (0.7705)	H O2 O1	1.00 (0.84) 0.49 (0.18) −0.49 (−0.05)
2m	0.7563 (0.7533)	O1 C7 H_{C7}	1.05 (0.87) −0.15 (−0.05) 0.06 (0.11)	**2m′**	0.7570 (0.7545)	O1 C7 C8	1.06 (0.73) −0.15 (−0.02) 0.03 (0.14)
3m	0.7560 (0.7541)	O2 C3 C4	1.04 (0.79) −0.14 (−0.05) 0.06 (0.14)	**3m′**	0.7563 (0.7548)	O2 C3 C4	1.04 (0.68) −0.14 (−0.04) 0.07 (0.20)
$TS_{2m'-3m'}$	0.8039 (0.7563)	O2 O1 H	0.65 (0.42) 0.63 (0.51) −0.21 (−0.03)	**TS_{2m-4m}**	0.7962 (0.7565)	C4 O1 Ht C5	0.85 (0.49) 0.59 (0.52) −0.23 (−0.04) −0.12 (−0.03)
4m	0.7632 (0.7538)	C4 C5 C3 Hnt	0.85 (0.98) −0.20 (−0.07) −0.16 (−0.05) −0.10 (−0.04)	**$TS_{3m'-11m}$**	0.8788 (0.7591)	C4 O2 C3 C5	0.92 (0.62) 0.64 (0.32) −0.44 (−0.04) −0.12 (−0.03)
11m	0.7630 (0.7538)	C4 C5 H_{C4} $H_{C4'}$	0.92 (1.05) −0.20 (−0.07) −0.11 (−0.05) −0.10 (−0.05)	**TS_{4m-5m}**	1.2317 (0.7663)	C4 H_{O2} O2 C5	0.91 (0.36) 0.98 (0.77) −0.69 (−0.10) −0.14 (−0.02)
TS_{4m-7m}	1.0447 (0.7534)	C4 O2 C3 C5	1.08 (0.11) 0.83 (0.85) −0.79 (−0.01) −0.16 (−0.01)	**11m′**	0.7628 (0.7538)	C4 C5 H_{C4} $H_{C4'}$	1.30 (1.08) −0.20 (−0.08) −0.11 (−0.05) −0.10 (−0.05)
$TS_{11m'-12m}$	0.9082 (0.7609)	C4 Ht O1 C5	0.82 (0.42) 0.72 (0.63) −0.39 (−0.06) −0.11 (−0.02)	**$TS_{3m'-13m}$**	0.9627 (0.7662)	O2 O9 C3	0.81 (0.39) 0.76 (0.60) −0.62 (−0.11)
13m	0.7572 (0.7551)	O9 C8 C7	1.05 (0.72) −0.15 (−0.03) 0.01 (0.16)	**13m′**	0.7562 (0.7548)	O9 C8 C7 H_{C8}	1.02 (0.67) −0.13 (−0.02) 0.06 (0.16) 0.05 (0.10)
$TS_{13m'-14m}$	1.1387 (0.7661)	O9 O13 O14 C8 C12 C7	0.81 (0.29) 0.80 (0.34) 0.45 (0.27) −0.69 (−0.06) −0.49 (−0.05) 0.10 (0.11)	**14m**	0.7564 (0.7559)	O13 O14	1.04 (0.56) −0.03 (0.51)
$TS_{13m'-16m}$	0.8112	O9 O1 H_{O1}	0.65 0.67 −0.23	**16m**	0.7565 (0.7545)	O1 C7 C8	1.05 (0.76) −0.15 (−0.03) 0.01 (0.14)
$TS_{16m-17m}$	0.926 (0.7598)	C8 O1 C7	0.76 (0.46) 0.70 (0.36) −0.57 (−0.02)	**17m**	0.7612 (0.7527)	C8	1.00 (0.84)
$TS_{17m-15m}$	0.9717 (0.7639)	H_{O9} C8 O9	0.81 (0.77) 0.78 (0.32) −0.54 (−0.11)	**$TS_{13m'-18m}$**	0.8850 (0.7572)	C7 O9 C8 C6	0.80 (0.35) 0.66 (0.42) −0.44 (0.00) −0.11 (−0.02)
18m	0.7606 (0.7534)	C7 C6 C10 O1	1.11 (0.82) −0.17 (−0.06) −0.15 (−0.04) 0.01 (0.09)	**$TS_{18m-17m}$**	0.7703 (0.7550)	C7 C8	0.52 (0.37) 0.50 (0.41)

[a] Spin densities (*S*) on selected atoms. The HF/3-21G and B3LYP/6-31G(d,p) values, in parenthesis, are shown.

O2; **TS_{2m-4m}** is associated to the Ht migration from C4 to O1, and **$TS_{3m'-11m}$** accounts for the C3−C4 breaking to render **11m**.

The O1 Radical Route: Obtention of 6m. Starting from the C4 secondary radical **4**, a two-step path has been proposed to render **6**, one of the major products experimentally obtained in the artemisinin decomposition (see Scheme 1). In the first step, the Fe(II) ion is released to obtain the epoxide species **5**, identified as a minor component in the products mixture in some artemisinin cleavage experiments. Then, the epoxide opening concerted with the lactone ring closure and the H migration from O1 to O2 would render the product **6**. We have theoretically modeled this pathway (Figure 3) from **4m**, via **TS_{4m-5m}**

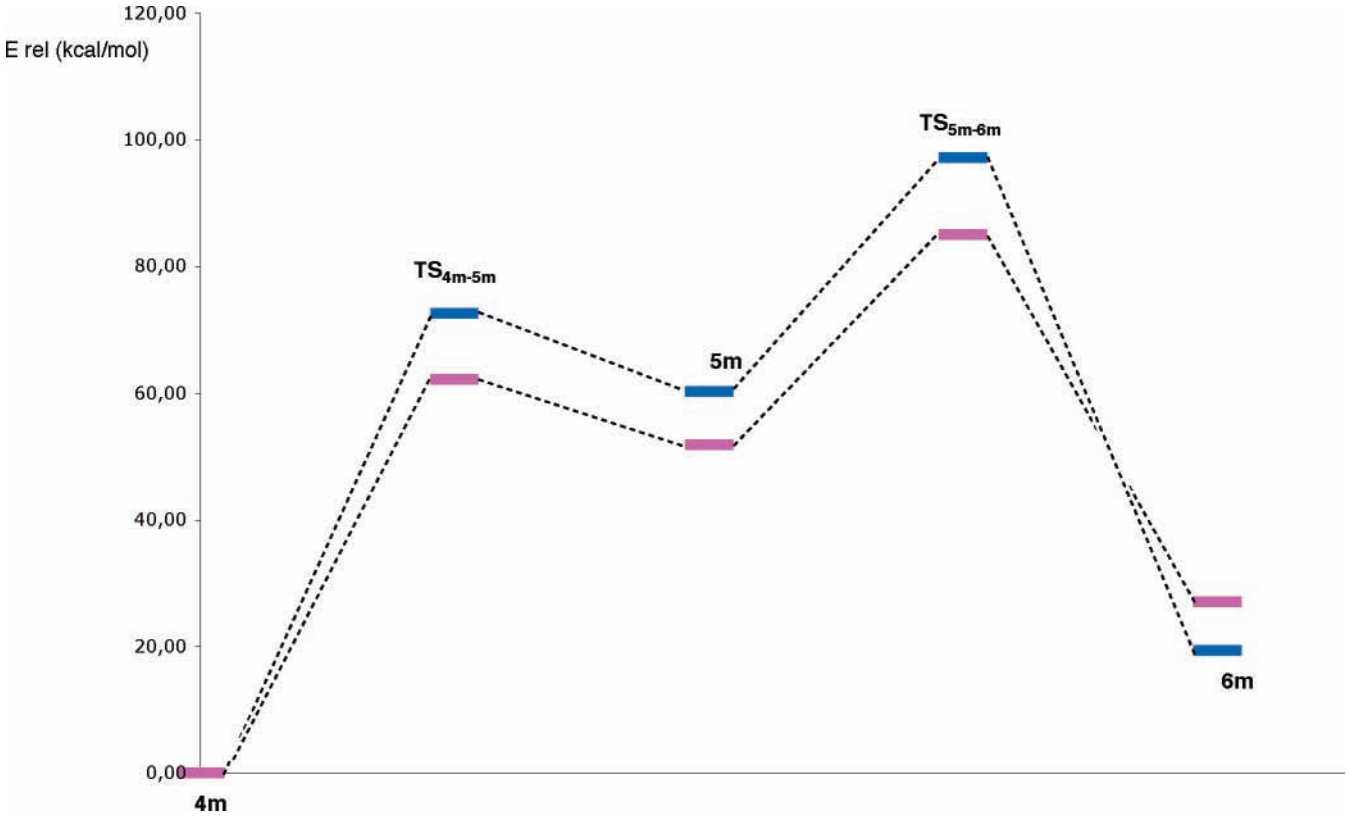

Figure 4. Energy profiles for the steps leading from **4m** to **6m**. HF and B3LYP results are indicated in blue and pink colors, respectively.

to obtain the epoxide intermediate **5m**, and then, through the $\mathbf{TS_{5m-6m}}$ describing the lactone closure and H_{O1} migration, **6m** is finally obtained.

The energetics of the calculated steps are detailed in the Supporting Information and depicted in Figure 4. The energy barrier for the first step is calculated to be quite high, around 62 kcal/mol (72.6 kcal/mol for the HF approach), which is not surprising because the epoxide intermediate plus an H atom was found to be ca. 52 kcal/mol (60 kcal/mol with HF) more unstable than the secondary radical **4m**. The epoxide intermediate opening, coupled to the H_{O1} shift from O1 to O2, occurs through a considerably lower energy barrier (around 33 kcal/mol), and the final product **6m** is hence attained. These results suggest that the epoxide intermediate would probably not be responsible for the antimalarial activity, because the O-centered and C-centered radicals are found to be more stable species. This observation is in agreement with the recent work by Taranto et al.[41]

The main components of the TV associated to $\mathbf{TS_{4m-5m}}$, reported as Supporting Information, describe the H_{O2} departure and O2−C4 closure. At the B3LYP level these two motions participate similarly, albeit antisymmetrically, in the TV. However, at the HF theoretical level, the H_{O2}−O2 distance is found to be very large, 2.21 Å, and hence the TV is dominated by the O2−C4 bond formation. It is worth noting that the H_{O2} that is eliminated from the model molecule is the H atom that entered at O2 in the first step of the global process and, hence, represents the Fe(II) ion in the real system. On the other hand, the TV associated to the $\mathbf{TS_{5m-6m}}$ does not show a clearly dominant component. Although the particular TV components values depend on the coordinates defined, the whole molecule participates in the epoxide opening and the final ring closure to yield **6m**.

The spin density at $\mathbf{TS_{4m-5m}}$ concentrates at H_{O2} and C4 (see Table 1, B3LYP values), and the species is properly described as having a doublet spin multiplicity. However, the HF/3-21G calculated wave function shows a large spin contamination, with an S^2 operator value of 1.2317, thus reinforcing the above observation that the B3LYP wave function offers a more accurate description of the calculated radicals.

The O1 Radical Route: Obtention of 8m. To account for the outcome of **8**, two alternative paths were proposed starting from **4**, see Scheme 1. One of them begins with the C3−O2 scission with O═Fe(IV) release, to yield the alkene **7**, that can be isomerized to render **8**. The other would start with a hydrogen abstraction from the media to render **9**, which, via the consecutive OFe^+ elimination and deprotonation, could give **8**. We have modeled the first proposed alternative (see Figure 5) with the $\mathbf{TS_{4m-7m}}$, which would account for the OH elimination (representing the O═Fe(IV) release), the **7m** alkene intermediate, and the isomerization to **8m** via the $\mathbf{TS_{7m-8m}}$.

However, we were not able to obtain a TS connecting **4m** and **9m**. Instead, we have taken into account that **4m** plus a hydrogen atom is a system with a global triplet multiplicity, while **9m** is a singlet. Thus, we have conducted a search for the minimum energy crossing point (MECP) between the triplet and singlet hypersurfaces in the vicinities of the structures of interest by means of the Harvey algorithm, that minimizes a generalized gradient obtained from the combination of the energies and gradients of the two potential energy surfaces that cross each other.[46] In such a way we have found the MECP reported in Figure 5, which can be taken as a representative point in the **4m**−**9m** step. From this MECP, an optimization in the singlet state renders **9m** which, via two alternative TSs describing the water elimination coupled with the ring closure (cf., $\mathbf{TS_{9m-8ma}}$ and $\mathbf{TS_{9m-8mb}}$) yields finally **8m** (plus water). It is worth noting that a species modeling **10** (see Scheme 1) could not be found within our model: the **9m**−**8m** conversion can be described by a single step with two alternatives depending on which oxygen is eliminated from the system to form the

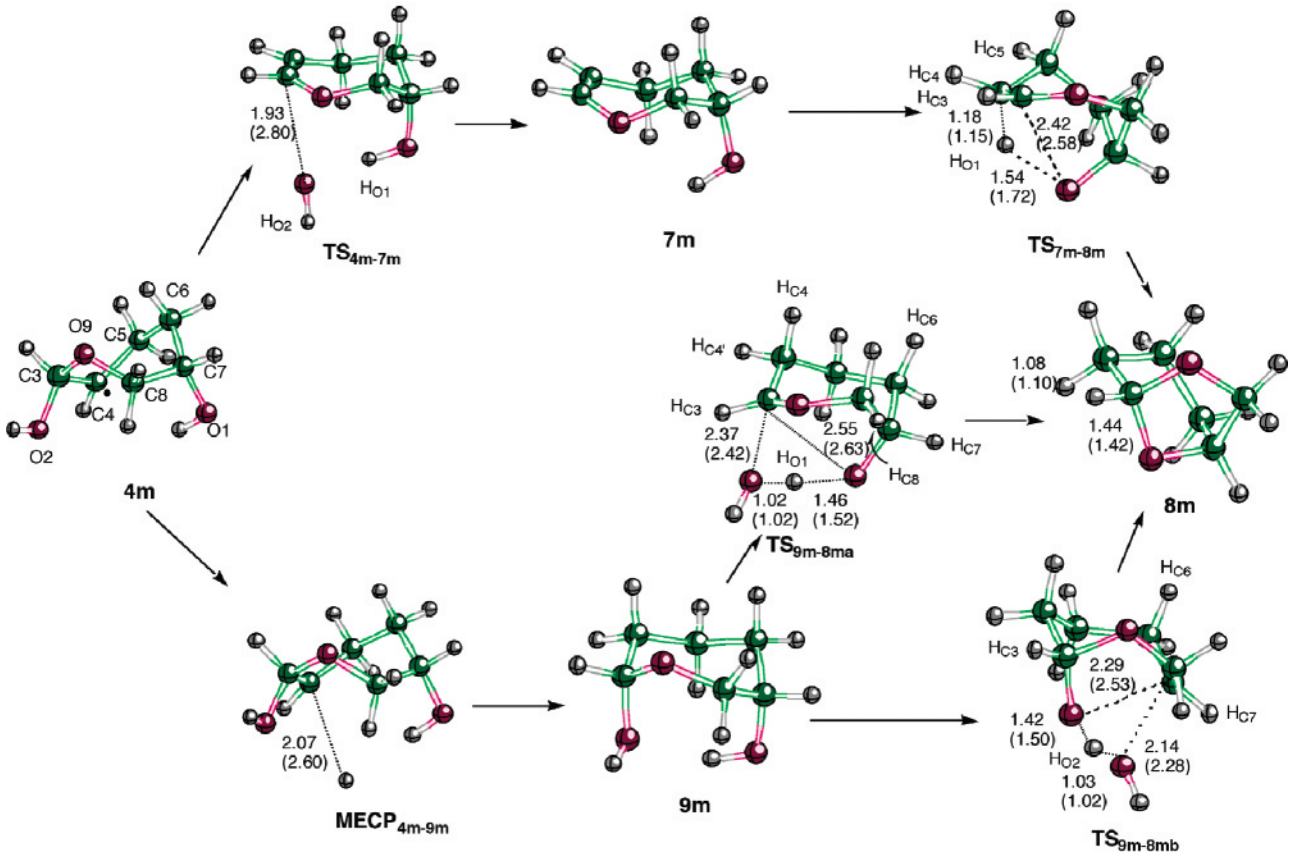

Figure 5. Structures obtained for **4m**, **7m**, **8m**, **9m**, $\mathbf{TS_{4m-7m}}$, $\mathbf{TS_{7m-8m}}$, $\mathbf{MECP_{4m-9m}}$, $\mathbf{TS_{9m-8ma}}$, and $\mathbf{TS_{9m-8mb}}$. Selected geometric distances (Å) at HF/3-21G and B3LYP/6-31G(d,p) (in parentheses) are shown. The atom numbering is also indicated.

water molecule (see Scheme 2). These two alternative steps would model an Fe(III)OH release to give the final product **8**.

It must be taken into account that the first pathway connects **4m** with **8m** plus a hydroxyl radical, while the second corresponds to the process from **4m** plus a hydrogen radical abstracted from the media, to give **8m** plus a water molecule. To make possible a comparison among the energetics of these points, we have added a water molecule representing the media from which an H atom is abstracted. In such a way, the two sequences would begin and end at the same points and comparisons can be done. The first step sequence would be as follows:

$$\mathbf{4m} + H_2O \rightarrow \mathbf{TS_{4m-7m}} + H_2O \rightarrow \mathbf{7m} + OH + H_2O \rightarrow \mathbf{TS_{7m-8m}} + OH + H_2O \rightarrow \mathbf{8m} + OH + H_2O$$

and the second sequence would be

$$\mathbf{4m} + H_2O \rightarrow \mathbf{4m} + H + OH \rightarrow \mathbf{MECP_{4m-9m}} + OH \rightarrow \mathbf{9m} + OH \rightarrow \mathbf{TSs_{9m-8m}} + OH \rightarrow \mathbf{8m} + OH + H_2O$$

In the first sequence the water molecule does not participate, and hence the relative energies have been calculated with respect to that of **4m**, without taking into account the water energy. At the beginning of the second sequence the water molecule is split into H and OH radicals, and the relative energies have been calculated with respect to that of **4m** plus a water molecule. In Figure 6 the energetic values obtained for these pathways are depicted. The highest point in the pathways from **4m** to **8m** is the $\mathbf{MECP_{4m-9m}}$ at the two calculation levels. This indicates that the first alternative path, via **7m**, would be preferred from a kinetic point of view, although the **9m** intermediate is more stable than the **7m** alkene and the TSs connecting **9m** with **8m** are also less energy demanding than the $\mathbf{TS_{7m-8m}}$. If there is a source of H in the medium the two proposed paths can compete, provided there is enough energy to surmount the barrier heights and reach **9**. The existence of two alternative paths ensures that **8** will be reached, as observed experimentally.

According to the main components of the TV (see the Supporting Information), the $\mathbf{TS_{4m-7m}}$ describes the OH release from the molecule, coupled with the C3−C4 double bond formation. The two theoretical levels render a rather different description: at the HF level the TV is largely dominated by the O2−C3 breaking bond, with a small contribution of the C3−C4 shortening. At B3LYP, on the contrary, a much larger O2−C3 distance is found so that the orientation of the OH fragment dominates the TV. Despite this different description, the IRC calculation from $\mathbf{TS_{4m-7m}}$ connects with the two proposed minima (**4m** and **7m**) at both theoretical levels. The $\mathbf{TS_{7m-8m}}$ shows a global fluctuation of the molecule, that is being rearranged to the bicyclic **8m** structure, and the H_{O1}−O1 distance as well as several dihedral angles describing the conformational change from the alkene to the bicycle contribute significantly to the TV.

As stated above, in the way from **4m** to **9m**, no TS is found. From **9m**, two alternative TSs can yield **8m**, depending on which oxygen leaves. The fluctuations are not limited to a particular fragment, but almost all the atoms in the molecule participate with its motions to the H_2O leaving to reach **8m**. Accordingly, the imaginary frequency values are low for $\mathbf{TS_{9m-8ma}}$ and $\mathbf{TS_{9m-8mb}}$.

As can be seen in Table 1, B3LYP results, the spin density at $\mathbf{TS_{4m-7m}}$ is mainly located at O2, because the OH fragment has almost been released from the molecule.

The O2 Radical Route: Obtention of 12m. Starting from the C4 primary radical **11**, a one-step path has been proposed

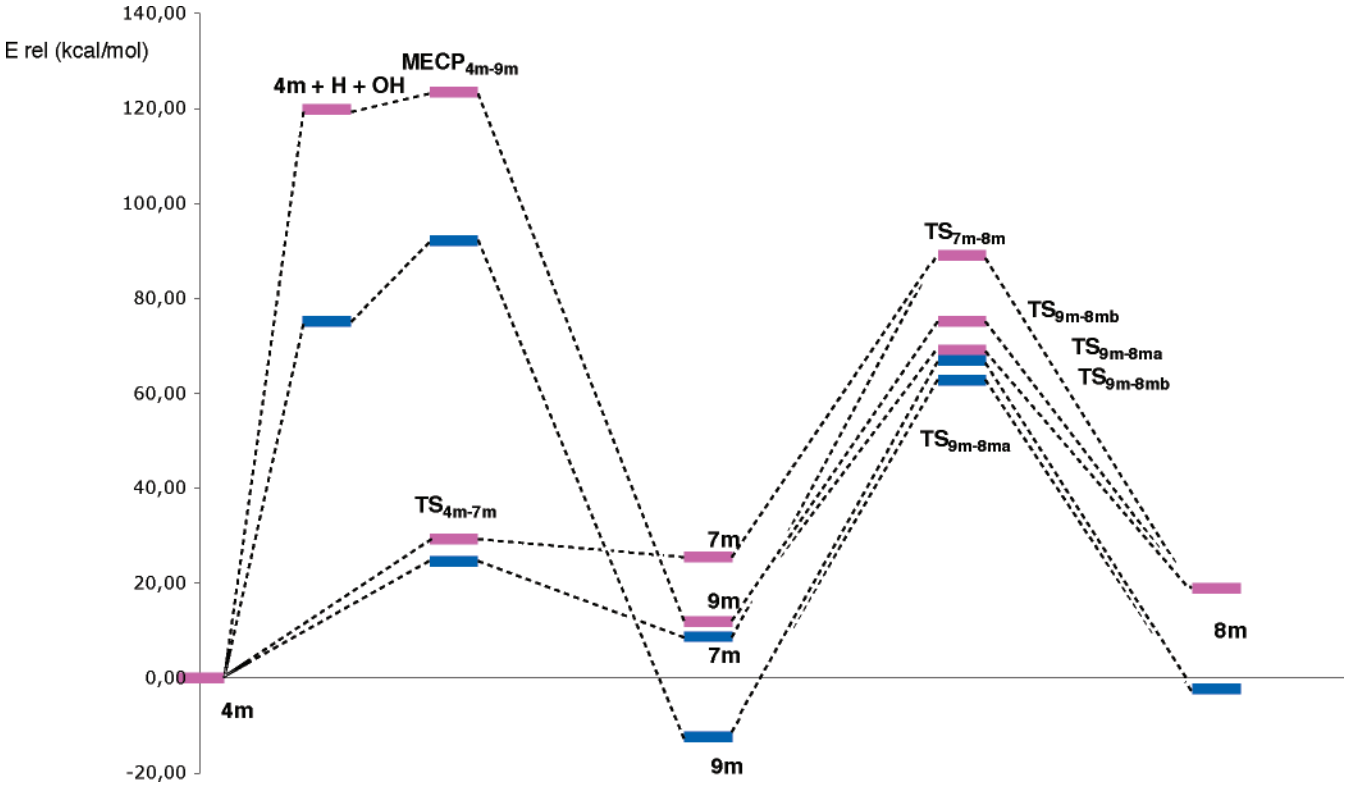

Figure 6. Energy profiles for the steps leading from **4m** to **8m**. HF and B3LYP results are indicated in blue and pink colors, respectively.

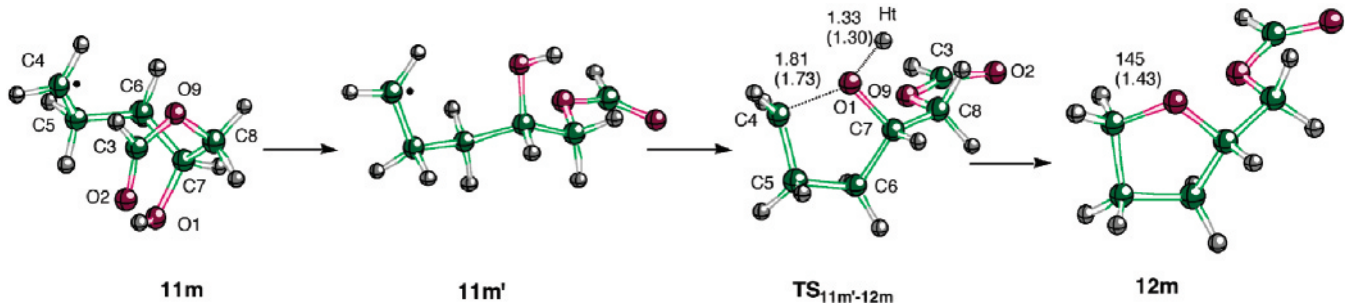

Figure 7. Structures obtained for **11m**, **11m′**, **12m**, and $\mathbf{TS}_{\mathbf{11m'-12m}}$. Selected geometric distances (Å) at HF/3-21G and B3LYP/6-31G(d,p) (in parentheses) are shown. The atom numbering is also indicated.

to render **12**, another product experimentally obtained in the artemisinin decomposition (see Scheme 1). In this step, the Fe(II) ion is released. We have modeled this pathway (Figure 7) from **11m**, via its conformer **11m′**, and $\mathbf{TS}_{\mathbf{11m'-12m}}$ to obtain **12m**. The conformational change between **11m** and **11m′** implies the loss of the weak intramolecular hydrogen bond between O1 and O2. Consequently, a slight energy increase of around 1 kcal/mol can be sensed. The $\mathbf{TS}_{\mathbf{11m'-12m}}$ is associated to the Ht (representing the Fe(II) ion) release from O1 and the coupled closure of the furane ring. The energetics of the calculated steps are detailed in the Supporting Information and depicted in Figure 8. The energy barrier for the step is calculated to be around 49 kcal/mol.

At the two theoretical levels, the main TV components for $\mathbf{TS}_{\mathbf{11m'-12m}}$ are the Ht−O1 distance and the C7−C6−C5 and O1−C7−C6 bond angles, thus reflecting the coupling between the closure of the ring and the Ht release. As expected, **11m** and **11m′** present a similar spin density distribution (see Table 1), with the unpaired electron localized at C4. At $\mathbf{TS}_{\mathbf{11m'-12m}}$, the spin density appears on Ht and C4, with a minor participation of O1.

The O2 Radical Route: from 3m to 14m. An alternative for the **3** radical decomposition was proposed to start with a C3−O9 scission, thus rendering the O9 radical **13** (see Scheme 1). Such species will be the intermediate to explain the appearance of **15** and other products derived either from **15** itself or from the oxygen radical **14**. Although these species are not the main products of the artemisinin decomposition, they have been sometimes detected in artemisinin derivatives decomposition studies.[47]

The first step, obtention of **13** from **3**, has been modeled to occur via **3m′** and $\mathbf{TS}_{\mathbf{3m'-13m}}$. In Figure 9 the structures of **3m′**, $\mathbf{TS}_{\mathbf{3m'-13m}}$, and **13m** are presented. The barrier height is quite low, around 14 kcal/mol, and thus this step would be a competitive pathway inside the O2 radical route. The energy values are reported as Supporting Information, and the energy profiles are depicted in Figure 10.

From **13m** onward the small molecular model used is not adequate, and it is necessary to enlarge it to include the neighbor six-membered ring, as can be seen in Scheme 2 (in which this neighbor ring is depicted in red color) and in Figure 9. The new model for **13** has been noted as **13m′**. The breaking of the O13−C8 bond, via $\mathbf{TS}_{\mathbf{13m'-14m}}$, would render the O radical **14m**. The barrier height associated to this step is around 22 kcal/mol.

The $\mathbf{TS}_{\mathbf{3m'-13m}}$ is clearly associated to the opening of the ring,

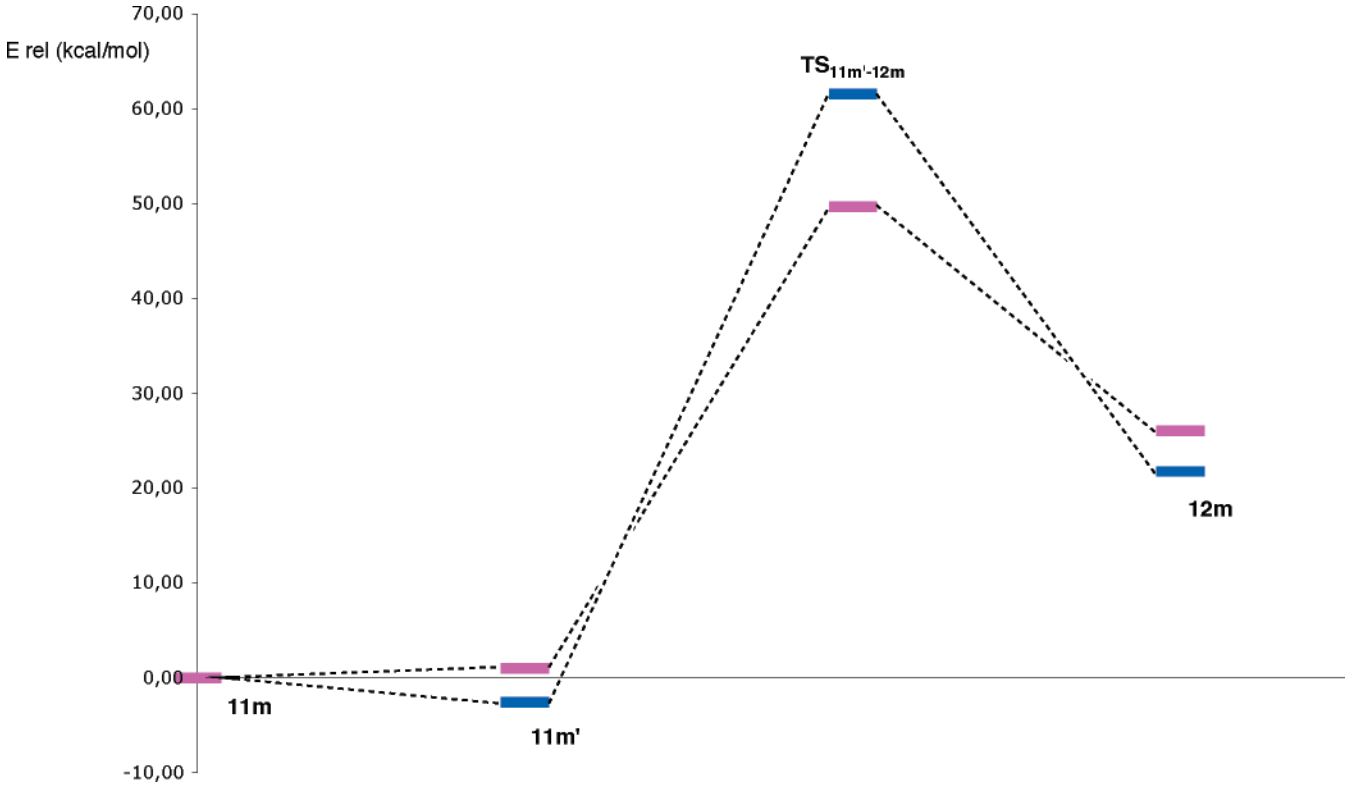

Figure 8. Energy profiles for the steps leading from **11m** to **12m**. HF and B3LYP results are indicated in blue and pink colors, respectively.

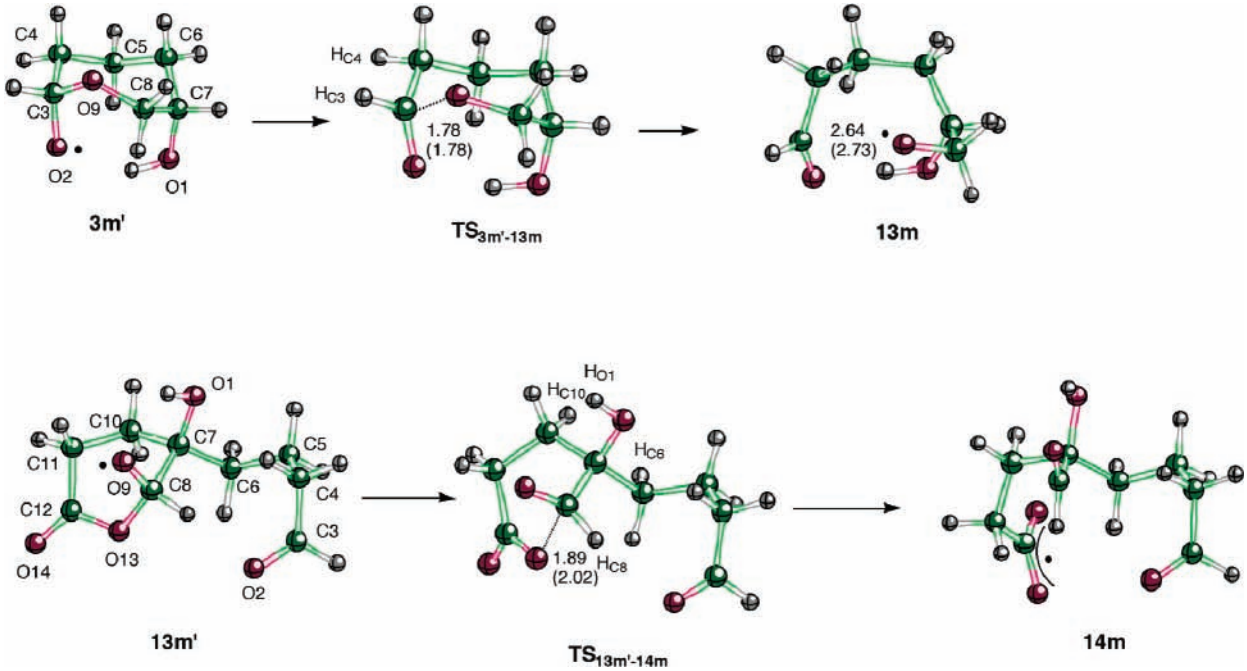

Figure 9. Structures obtained for **3m′**, **13m**, **13m′**, **14m**, $TS_{3m'-13m}$, and $TS_{13m'-14m}$. Selected geometric distances (Å) at HF/3-21G and B3LYP/6-31G(d,p) (in parentheses) are shown. The atom numbering is also indicated.

with a significant participation of the O2−C3 bond, that evolves to a double bond in **13m**, and angles and dihedrals related with the ring opening. The main component in the TV associated to $TS_{13m'-14m}$ is the O13−C8 bond distance that is being broken, with some angles and dihedrals participating also in the TV because of the second ring opening taking place at this point.

At $TS_{3m'-13m}$ the spin density can be found partitioned between O2 and O9 (see Table 1), with some negative participation of C3. Once **13m** is reached, the unpaired electron is located on O9 with a small delocalization to C7. At **13m′** the same trend is found, with the only difference that H_{C8} also participate in the electron delocalization. Then, at $TS_{13m'-14m}$, a strong delocalization of the unpaired electron is found, and the spin density is widespread on O9, O13, O14, and C7. C8 and C12 are found to have some (negative) spin density, especially at the HF level. Finally, at **14m**, the unpaired electron is delocalized between O13 and O14 (B3LYP results; at the HF level this electron is wrongly assigned to O13).

The O2 Radical Route: Obtention of 15m. From **13**, another pathway has been proposed: a C7−C8 scission with

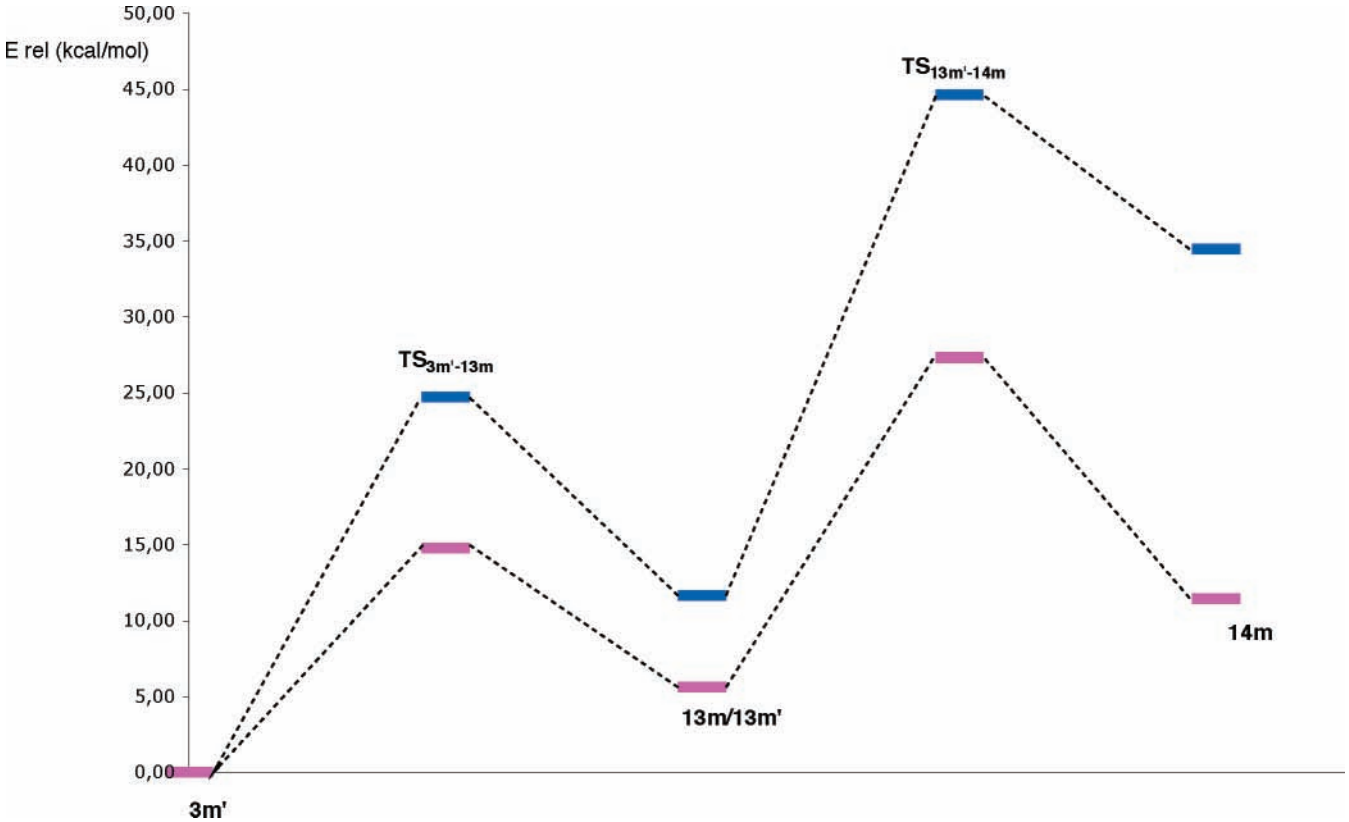

Figure 10. Energy profiles for the steps leading from **3m′** to **14m**. HF and B3LYP results are indicated in blue and pink colors, respectively.

Fe(II) release would render the final species **15** and derived products (Scheme 1). However, we have found that this pathway is not a single step. Instead, two alternative pathways have been calculated starting from **13m′** and ending up at **15m** (Scheme 2): the first one would start with the C7−C8 breaking (via $\mathbf{TS_{13m'-18m}}$) to render the C7 radical **18m**, which in turn would suffer an intramolecular hydrogen transfer between O1 and O9 through $\mathbf{TS_{18m-17m}}$, yielding the C8 radical **17m**. It is worth noting that the H motion from O1 to O9 represents the Fe(III) motion in the real system. The second one would start with the H migration from O1 to O9 through the $\mathbf{TS_{13m'-16m}}$, yielding the O1 radical **16m**. Then the C7−C8 bond breaking would take place, via $\mathbf{TS_{16m-17m}}$, and in this way **17m** is obtained again. This second alternative pathway was not completely characterized by using the B3LYP/6-31G(d,p) calculation level, because all efforts to find the $\mathbf{TS_{13m'-16m}}$ were unsuccessful. However, the $\mathbf{TS_{16m-17m}}$ has also been obtained by using the B3LYP approach. Once **17m** was reached, the H release from O9, representing the Fe(II) release, via $\mathbf{TS_{17m-15m}}$, would give the final product **15m**.

These structures are depicted in Figure 11, and the corresponding energies are reported as Supporting Information and drawn in Figure 12. It is apparent that the pathway through **18m** is preferred, according to the B3LYP results. However, the HF/3-21G calculations suggest an initial preference for the pathway through **16m** despite the higher energy barrier via $\mathbf{TS_{13m'-16m}}$ if compared with the transit through $\mathbf{TS_{13m'-18m}}$, because the second step from **18m** to **17m** is more energy demanding. At the two theoretical levels, the highest point in the energy profiles is found to be $\mathbf{TS_{17m-15m}}$, and hence if **15m** is to be reached, the two pathways will compete.

The main TV components correlate well with the expected atom motions in all cases: $\mathbf{TS_{13m'-18m}}$ is mainly associated with the C8−C7 bond breaking, and the TV associated with $\mathbf{TS_{18m-17m}}$ is dominated by the Ht−O1 distance and, to a lesser extent, by the O1−C7 and O9−C8 bonds evolving from single to double and from double to single, respectively. The $\mathbf{TS_{17m-15m}}$ describes the H_{O9} departure coupled with the O9−C8 bond that evolves to a carbonylic bond at **15m**. On the other hand, at the $\mathbf{TS_{13m'-16m}}$ it can be sensed that the H_{O1}−O9 distance that is being shortened and the angles describing the conformation around the C7−C8 bond participate significantly in the associated TV. The $\mathbf{TS_{16m-17m}}$ is mainly associated with the C8−C7 bond breaking.

The results shown in Table 1 for $\mathbf{TS_{13m'-16m}}$ describe a partitioning of the spin density between O9 and O1, with a smaller and negative value for the H_{O1} being transferred. At **16m** the unpaired electron is found at O1, as expected, and at **17m** the spin density is found at C8. The $\mathbf{TS_{16m-17m}}$ shows an intermediate situation with the unpaired electron delocalized between O1 and C8. On going from **17m** to **15m** the unpaired electron moves to H_{O9}, that will be released as a hydrogen atom in our model system.

The second pathway from **13m′** begins with $\mathbf{TS_{13m'-18m}}$, in which the unpaired electron is moving from O9 to C7. At **18m** the spin density is found at C7, as expected, and the $\mathbf{TS_{18m-17m}}$ shows a delocalization of the unpaired electron between C7 and C8, with no remarkable spin density found on O9, O1, or Ht.

Overall Overview: The Whole Set of Mechanisms. Up to this point, we have reported the results step by step. To obtain a global view of the processes studied, it is very convenient to assemble the fragments. In Figure 13, a global energy profile is drawn starting from **1m**, describing the O1 radical route up to the final products **6m** and **8m**, as obtained by using the B3LYP/6-31G(d,p) theoretical level. This view reveals that the two products are very close in energy to each other, and the same can be said about the points of maximum energy in the pathways of minimum energy connecting the reactants to each one of the products, cf., $\mathbf{TS_{5m-6m}}$ and $\mathbf{TS_{7m-8m}}$ for the routes to **6m** and **8m**, respectively. Also, it is interesting to note that

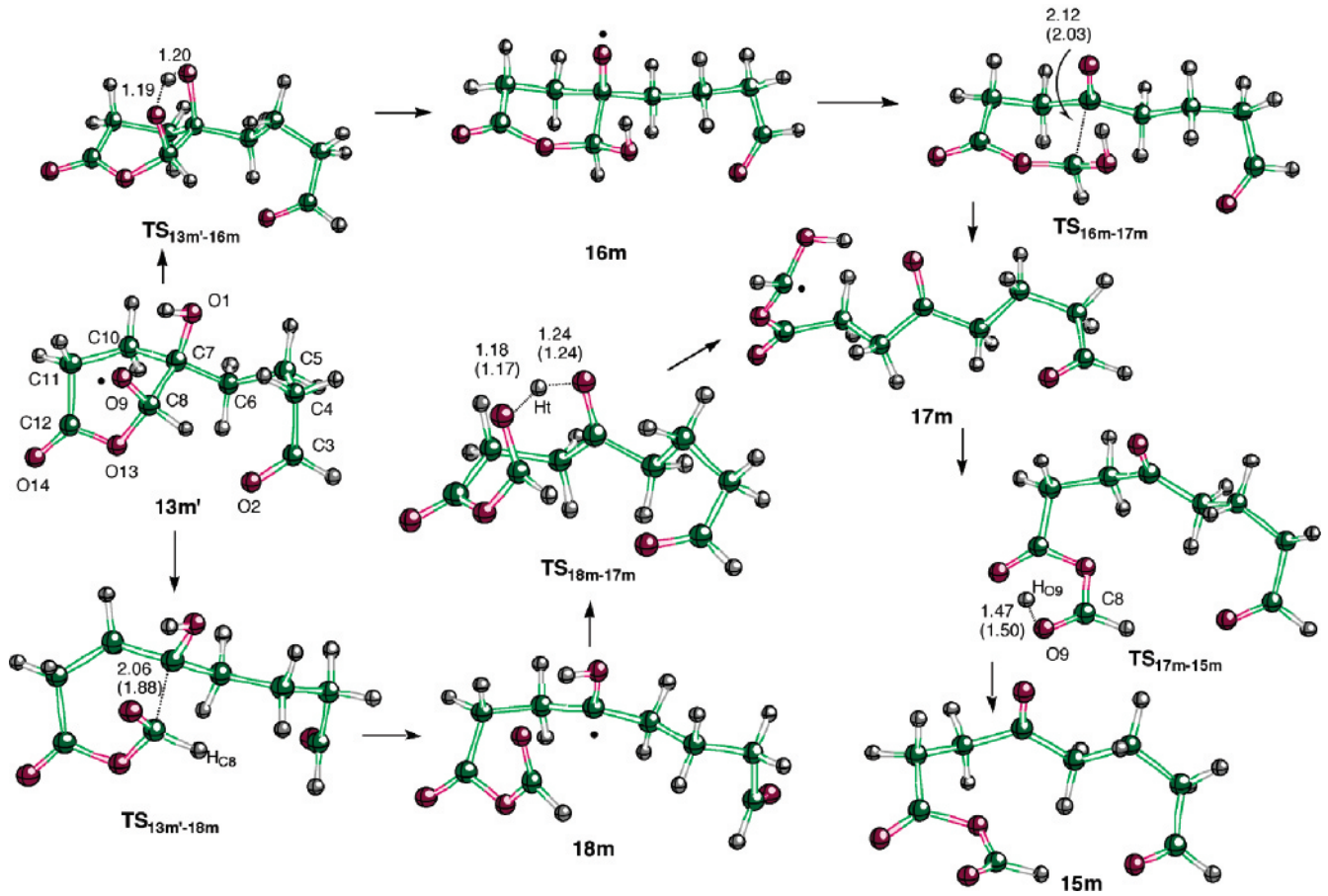

Figure 11. Structures obtained for **13m′**, **16m**, **17m**, **18m**, **15m**, $TS_{13m'-16m}$, $TS_{16m-17m}$, $TS_{13m'-18m}$, $TS_{18m-17m}$, and $TS_{17m-15m}$. Selected geometric distances (Å) at HF/3-21G and B3LYP/6-31G(d,p) (in parentheses) are shown. The atom numbering is also indicated.

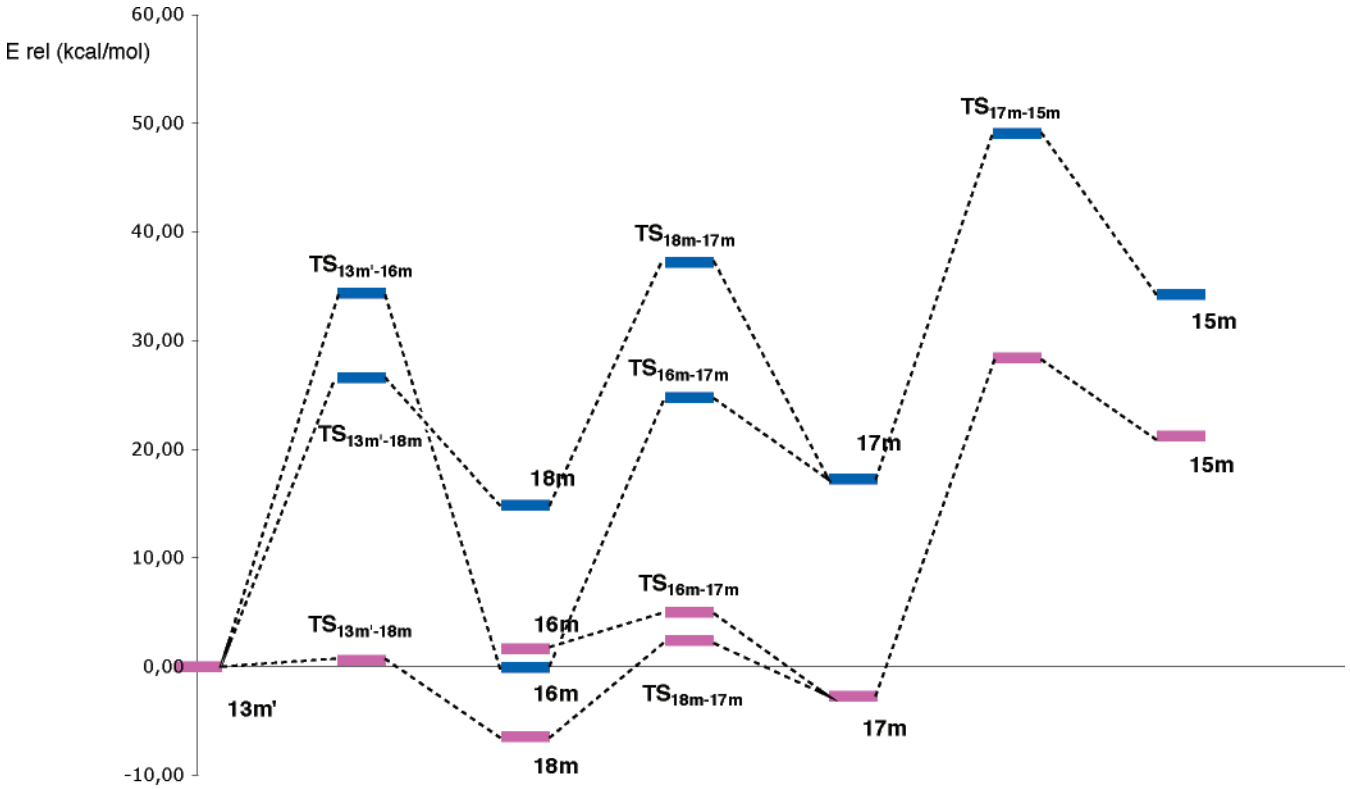

Figure 12. Energy profiles for the steps leading from **13m′** to **15m**. HF and B3LYP results are indicated in blue and pink colors, respectively.

almost all points in the reported routes lie under the energy value of the initial TS, thus ensuring the products formation if the reaction is initiated: the competition between the paths will be resolved mainly as a function of the experimental conditions,

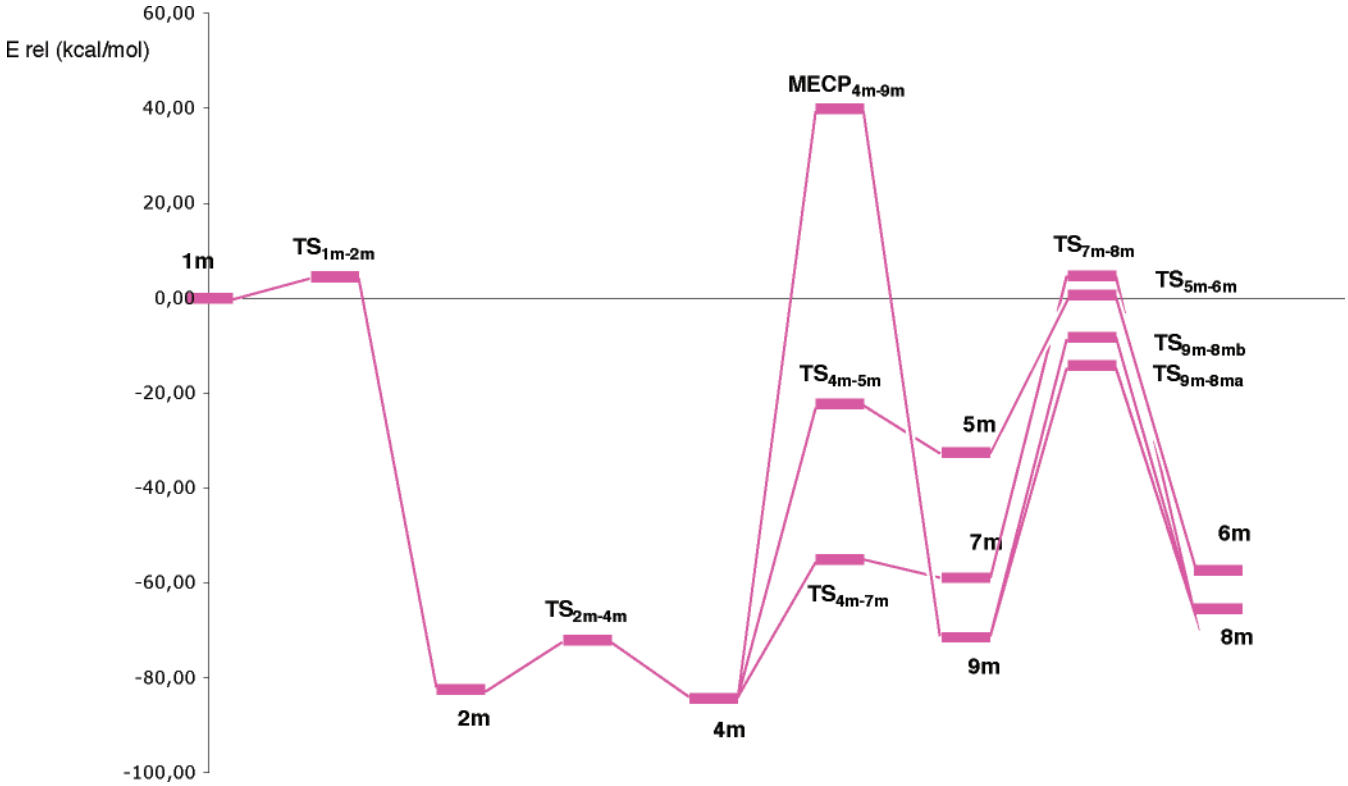

Figure 13. Energy profiles for the O1 radical route, calculated at the B3LYP/6-31 G(d,p) level.

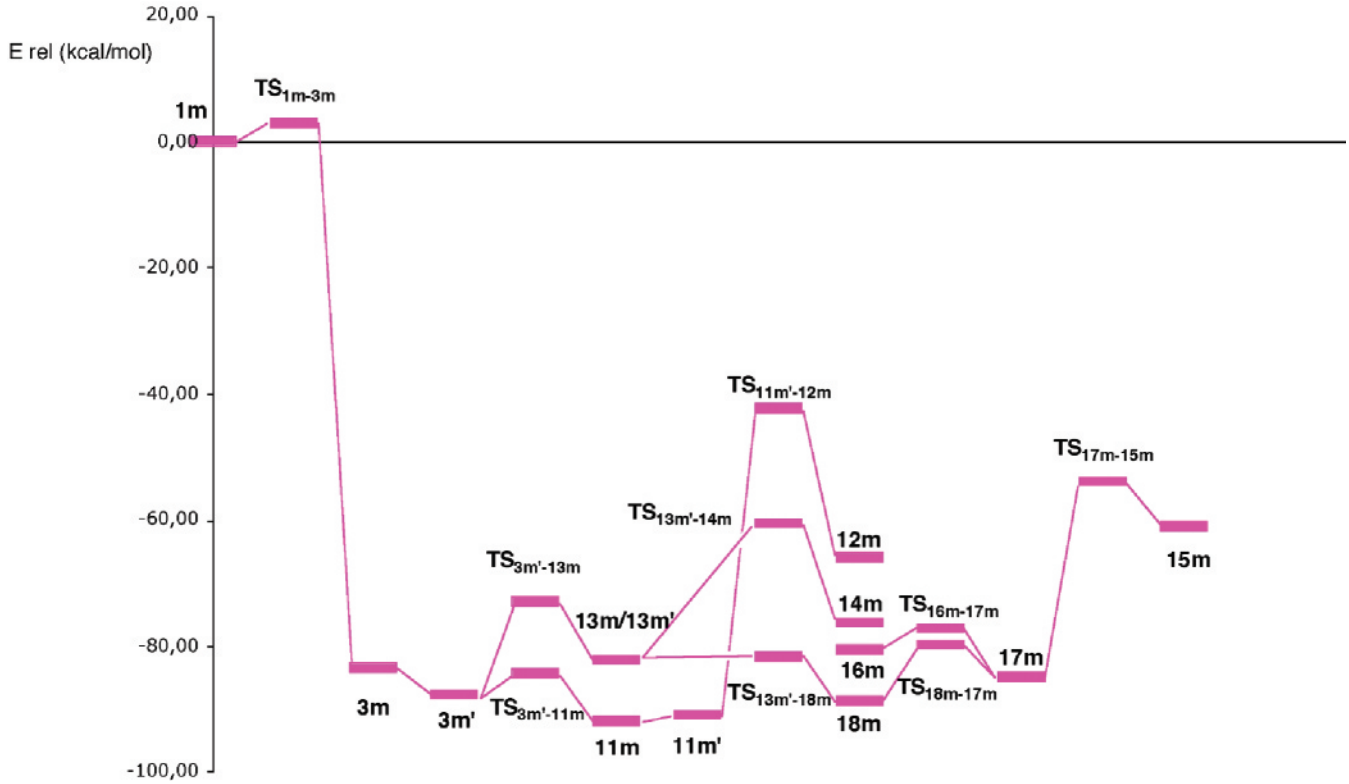

Figure 14. Energy profiles for the O2 radical route, calculated at the B3LYP/6-31 G(d,p) level.

and hence one or the other product will be found as the major one. As can be seen, the **MECP**$_{4m-9m}$ point lies at a relatively high energy, and as stated above the obtention of **8m** is better explained via **7m** and **TS**$_{7m-8m}$.

In Figure 14, the global energy profile is drawn starting from **1m**, describing this time the O2 radical route up to the final products **12m** and **15m**. It must be said that **14m** is not a final product, but a radical that would further evolve to other species not studied here. Again it is revealed that the two products are very close in energy to each other, although in this case there is a larger difference between the energies of the points of maximum energy in the pathways of minimum energy connecting the reactants to each one of the products, cf., **TS**$_{11m'-12m}$ and **TS**$_{17m-15m}$ for the routes to **12m** and **15m**, respectively.

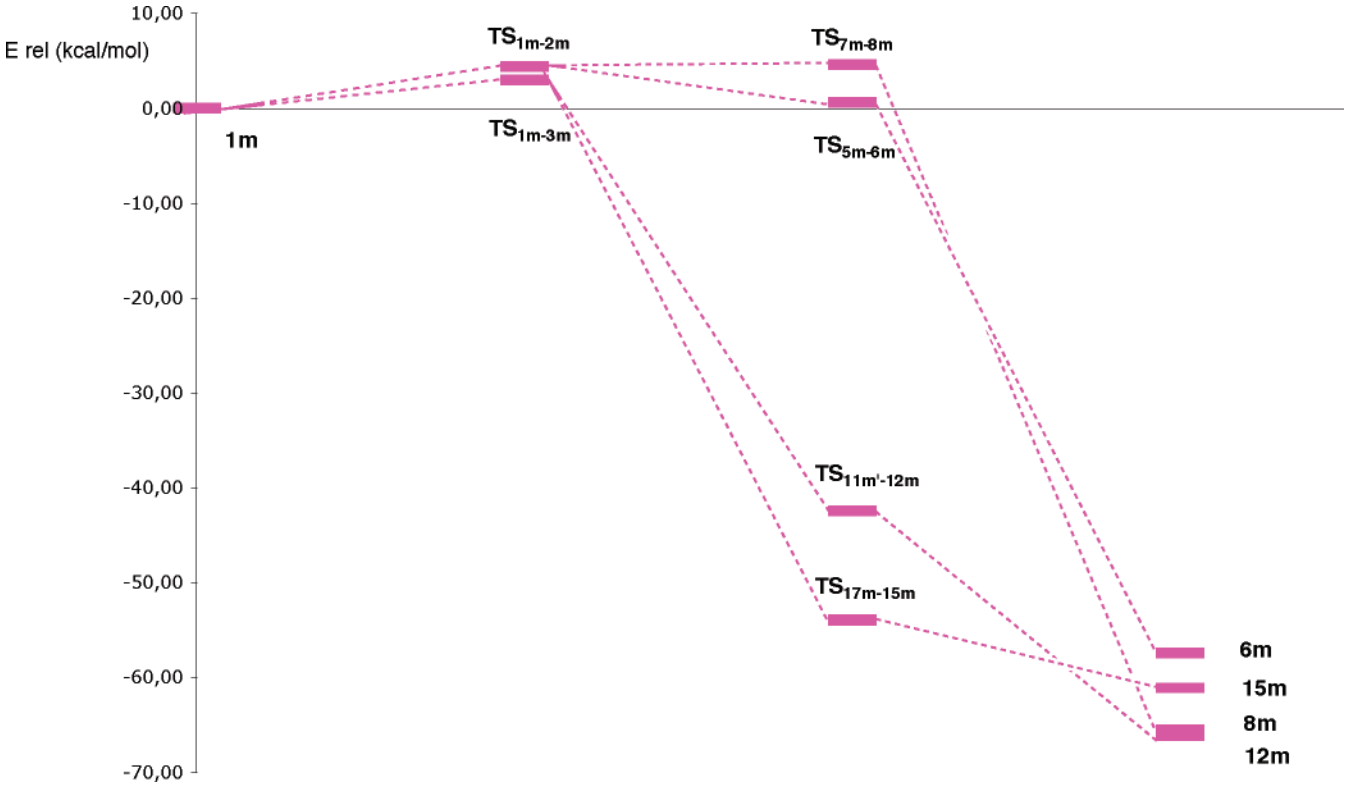

Figure 15. Comparative energies of the reactants, the initial TSs, the stationary points of highest energy found along the minimum energy pathways studied, and the species modeling the experimentally obtained products, as calculated by means of the B3LYP/6-31G(d,p) theoretical level.

All points in the reported routes lie under the energy value of the initial TS, and the products formation and the competition between the paths would take place, as before.

The aforementioned observations are even clearer in Figure 15, in which only the starting reactants, the initial TSs, the TSs of maximum energy along the minimum energy O1 and O2 radical routes, and the final products are sketched. From this figure it can be seen that the products **12m** and **15m** are predicted to be formed in an easier way, and that the formation of **8m** and **6m** is also straightforward once the reaction is initiated, because the highest point to surmount is the initial TS for all cases except the **8m** obtention, for which a very small increase in energy of only 0.20 kcal/mol is found until $\mathbf{TS_{7m-8m}}$ is reached.

Conclusions

The main goal of the work herein reported was to substantiate from a theoretical point of view the suggested molecular mechanisms for the artemisinin decomposition. By using a relatively simple molecular model and two theoretical approaches, we have found that the appearance of the final products can be explained in a satisfactory way. Furthermore, several intermediates and radicals have been found as relatively stable species, thus giving support to the current hypothesis that some of such species can be responsible for the antimalarial action of artemisinin and its derivatives, either by hitting specific targets within the parasite or by disrupting the hemozoin polymerization process and causing in this way the *Plasmodium* death.

Further work is guaranteed in what concerns the description of the model system, and our group is conducting calculations on the artemisinin decomposition process with more accurate models, including on one hand the Fe(II) ion that initiates the cascade of reactions from the artemisinin to the final products and on the other the solvent effects that can be determinant in discriminating between the possible pathways. The way by which the potentially antimalarial intermediates hit the putative targets, and the effect of the different substituents in the artemisinin derivatives, are also under study.

Despite the simple model and moderate theoretical levels used, some specific conclusions can be derived from this work:

(a) The products formation is assured once the reaction is initiated, and the different paths will compete depending on the experimental conditions.

(b) We have for the first time obtained a TS modeling the previously postulated interconversion between the initial O-centered radicals. With this finding, it has been demonstrated that the O1 and O2 radical routes are intimately related.

(c) The epoxide intermediate is probably not responsible for the antimalarial activity, because other intermediates are found to be more stable and potentially more active as alkylating agents. This is in agreement with the recent work by Taranto et al.[41]

(d) The formation of **8**(**m**) can take place via two different mechanisms, but the preferred pathway will be the one passing through **7**(**m**).

(e) The formation of **15**(**m**) is a process more complex than originally suggested and involves three different steps from the oxygen-centered radical **13**(**m**).

(f) Although the two theoretical approaches used render similar values for the geometric parameters, some significant differences are found in what concerns the energies and fluctuation patterns, as well as the description of the spin distribution in the molecule. The B3LYP/6-31G(d,p) calculations are preferred for a reasonable calculation of the last properties.

(g) One of the stationary points ($\mathbf{TS_{13m'-16m}}$) was found at the HF/3-21G level, but not by using the B3LYP/6-31G(d,p)

calculations. This fact could suggest that actually only one of the paths herein studied connecting **13m′** with **18m** takes place.

The present paper has to be understood as an extension of the pioneering works by Gu et al.[7] and Taranto et al.[8] in this field and opens a broad investigation project to further efforts that will hopefully contribute to a better understanding of the antimalarial activity of artemisinin and its derivatives.

Acknowledgment. Financial support by the Generalitat Valenciana (Project GV04B-029) and Fundació Bancaixa-UJI (P1 1A2002-04 and P1 1B2005-15) is gratefully acknowledged. P.M. acknowledges the Generalitat Valenciana for the Grant TS/05/UJI/02.

Supporting Information Available: Tables containing the absolute and relative energies of the stationary points found at both theoretical levels used; Tables containing the imaginary frequencies, the unique negative eigenvalues, and the main components of the TVs for the TSs obtained at both theoretical levels used; selected geometric parameters. This material is available free of charge via the Internet at http://pubs.acs.org.

References and Notes

(1) Meshnick, S. R.; Taylor, T. E.; Kamchonwongpaisan, S. *Microbiol. Rev.* **1996**, *60*, 301.

(2) Pinheiro, J. C.; Kiralj, R.; Ferreira, M. C. *QSAR Comb. Sci.* **2003**, *22*, 830.

(3) O'Neill, P. M.; Posner, G. H. *J. Med. Chem.* **2004**, *47*, 2945.

(4) Posner, G. H.; O'Neill, P. M. *Acc. Chem. Res.* **2004**, *37*, 397.

(5) Klayman, D. L. *Science* **1985**, *228*, 1049.

(6) Haynes, R. K.; Ho, W.-Y.; Chan, H.-W.; Fugmann, B.; Stetter, J.; Croft, S. L.; Vivas, L.; Peters, W.; Robinson, B. L. *Angew. Chem., Int. Ed.* **2004**, *43*, 1381.

(7) Gu, J.; Chen, K.; Jiang, H.; Leszczynski, J. *J. Phys. Chem. A* **1999**, *103*, 9364.

(8) Taranto, A. G.; Carneiro, J. W. d. M.; de Oliveira, F. G.; de Araujo, M. T.; Correa, C. R. *J. Mol. Struct.: THEOCHEM* **2002**, *580*, 207.

(9) Robert, A.; Dechy-Cabaret, O.; Cazelles, J.; Meunier, B. *Acc. Chem. Res.* **2002**, *35*, 167.

(10) Krungkrai, S. R.; Yuthavong, Y. *Trans. R. Soc. Trop. Med. Hyg.* **1987**, *81*, 710.

(11) Meshnick, S. R. *Lancet* **1994**, *344*, 1441.

(12) Eckstein-Ludwig, U.; Webb, R. J.; van Goethem, I. D. A.; East, J. M.; Lee, A. G.; Kimura, M.; O'Neill, P. M.; Bray, P. G.; Ward, S. A.; Krishna, S. *Nature* **2003**, *424*, 957.

(13) Haynes, R. K.; Pai, H. H.-O.; Voerste, A. *Tetrahedron Lett.* **1999**, *40*, 4715.

(14) Cazelles, J.; Robert, A.; Meunier, B. *J. Org. Chem.* **1999**, *64*, 6776.

(15) Cumming, J. N.; Ploypradith, P.; Posner, G. H. *Adv. Pharmacol.* **1996**, *37*, 253.

(16) Robert, A.; Meunier, B. *Chem. Soc. Rev.* **1998**, *27*, 273.

(17) Jefford, C. W.; Vicente, M. G. H.; Jacquier, Y.; Faverger, F.; Mareda, J.; Millason-Schmidt, P.; Brunner, G.; Burger, U. *Helv. Chim. Acta* **1996**, *79*, 1475.

(18) Jefford, C. W. *Curr. Med. Chem.* **2001**, *8*, 1803.

(19) Meshnick, S. R.; Thomas, A.; Ranz, A.; Xu, C. M.; Pan, H. Z. *Mol. Biochem. Parasitol.* **1991**, *49*, 181.

(20) Posner, G. H.; Oh, C. H. *J. Am. Chem. Soc.* **1992**, *114*, 8328.

(21) Wu, Y. *Acc. Chem. Res.* **2002**, *35*, 255.

(22) Butler, A. R.; Gilbert, B. C.; Hulme, P.; Irvine, L. R.; Renton, L.; Whitwood, A. C. *Free Radical Res.* **1998**, *28*, 471.

(23) Wu, W.-M.; Wu, Y.; Wu, Y.-L.; Yao, Z.-J.; Zhou, C.-M.; Li, Y.; Shan, F. *J. Am. Chem. Soc.* **1998**, *120*, 3316.

(24) O'Neill, P. M.; Bishop, L. P.; Searle, N. L.; Maggs, J. L.; Ward, S. A.; Park, B. K.; Mabbs, F. *J. Org. Chem.* **2000**, *65*, 1578.

(25) Szpilman, A. M.; Korshin, E. E.; Hoos, R.; Posner, G. H.; Bachi, M. D. *J. Org. Chem.* **2001**, *66*, 6531.

(26) Zhang, F.; Gosser, D. K.; Meshnick, S. R. *Biochem. Pharmacol.* **1992**, *43*, 1805.

(27) Robert, A.; Cazelles, J.; Meunier, B. *Angew. Chem., Int. Ed.* **2001**, *40*, 1954.

(28) Cazelles, J.; Robert, A.; Meunier, B. *J. Org. Chem.* **2002**, *67*, 609.

(29) Olliaro, P.; Haynes, R. K.; Meunier, B.; Yongyuth, Y. *Trends Parasitol.* **2001**, *17*, 123.

(30) Ridley, R. G. *Nature* **2003**, *424*, 887.

(31) Haynes, R. K.; Monti, D.; Taramelli, D.; Basilico, N.; Parapini, S.; Olliaro, P. *Antimicrob. Agents Chemother.* **2003**, *47*, 1175.

(32) Yang, Y. Z.; Asawamahasakda, W.; Meshnick, S. R. *Biochem. Pharmacol.* **1993**, *46*, 336.

(33) Yang, Y. Z.; Little, B.; Meshnick, S. R. *Biochem. Pharmacol.* **1994**, *48*, 569.

(34) Asawamahasakda, W.; Ittarat, I.; Pu, Y. M.; Ziffer, H.; Meshnick, S. R. *Antimicrob. Agents Chemother.* **1994**, *38*, 1854.

(35) Bhisutthibhan, J.; Philbert, M. A.; Fujioka, H.; Aikawa, M.; Meshnick, S. R. *Eur. J. Cell. Biol.* **1994**, *78*, 665.

(36) Bhisutthibhan, J.; Meshnick, S. R. *Antimicrob. Agents Chemother.* **2001**, *45*, 2397.

(37) Pandey, A. V.; Tekwani, B. L.; Singh, R. L.; Chauhan, V. S. *J. Biol. Chem.* **1999**, *274*, 19383.

(38) Drew, M. G. B.; Metcalfe, J.; Ismail, F. M. D. *J. Mol. Struct.: THEOCHEM* **2004**, *711*, 95.

(39) Tonmunphean, S.; Parasuk, V.; Kokpol, S. *J. Mol. Struct.: THEOCHEM* **2005**, *724*, 99.

(40) Arantes, C.; de Araujo, M. J.; Taranto, A. G.; de Carneiro, J. W. *Int. J. Quantum Chem.* **2005**, *103*, 749.

(41) Taranto, A. G.; Carneiro, J. W. d. M.; de Araujo, M. T. *Bioorg. Med. Chem.* **2006**, *14*, 1546.

(42) McIver, J. W., Jr. *Acc. Chem. Res.* **1974**, *7*, 72.

(43) Fukui, K. *J. Phys. Chem.* **1970**, *74*, 4161.

(44) Frisch, M. J.; Trucks, G. W.; Schlegel, H. B.; Scuseria, G. E.; Robb, M. A.; Cheeseman, J. R.; Zakrzewski, V. G.; Montgomery, J. A., Jr.; Stratmann, R. E.; Burant, J. C.; Dapprich, S.; Millam, J. M.; Daniels, A. D.; Kudin, K. N.; Strain, M. C.; Farkas, O.; Tomasi, J.; Barone, V.; Cossi, M.; Cammi, R.; Mennucci, B.; Pomelli, C.; Adamo, C.; Clifford, S.; Ochterski, J.; Petersson, G. A.; Ayala, P. Y.; Cui, Q.; Morokuma, K.; Malick, D. K.; Rabuck, A. D.; Raghavachari, K.; Foresman, J. B.; Cioslowski, J.; Ortiz, J. V.; Baboul, A. G.; Stefanov, B. B.; Liu, G.; Liashenko, A.; Piskorz, P.; Komaromi, I.; Gomperts, R.; Martin, R. L.; Fox, D. J.; Keith, T.; Al-Laham, M. A.; Peng, C. Y.; Nanayakkara, A.; Gonzalez, C.; Challacombe, M.; Gill, P. M. W.; Johnson, B.; Chen, W.; Wong, M. W.; Andres, J. L.; Gonzalez, C.; Head-Gordon, M.; Replogle, E. S.; Pople, J. A. *Gaussian 98*, revision A.7 ed.; Gaussian, Inc.: Pittsburgh, PA, 1998.

(45) Posner, G. H.; Cumming, J. N.; Ploypradith, P.; Oh, C. H. *J. Am. Chem. Soc.* **1995**, *117*, 5885.

(46) Harvey, J. N.; Ascgi, M.; Schwarz, H.; Koch, W. *Theor. Chem. Acc.* **1998**, *99*, 95.

(47) Avery, M. A.; Fan, P.-C.; Karle, J. M.; Bonk, J. D.; Miller, R.; Goins, D. K. *J. Med. Chem.* **1996**, *39*, 1885.